

THE COS-HALOS SURVEY: PHYSICAL CONDITIONS AND BARYONIC MASS IN THE LOW-REDSHIFT CIRCUMGALACTIC MEDIUM

JESSICA K. WERK^{1,11}, J. XAVIER PROCHASKA¹, JASON TUMLINSON², MOLLY S. PEEPLES², TODD M. TRIPP³, ANDREW J. FOX², NICOLAS LEHNER⁴, CHRISTOPHER THOM², JOHN M. O’MEARA⁵, AMANDA BRADY FORD⁶, RONGMON BORDOLOI², NEAL KATZ³, NICOLAS TEJOS¹, BENJAMIN D. OPPENHEIMER^{7,8}, ROMEEL DAVÉ⁹, AND DAVID H. WEINBERG¹⁰

¹ UCO/Lick Observatory; University of California, Santa Cruz, CA, USA; jwerk@ucolick.org

² Space Telescope Science Institute, 3700 San Martin Drive, Baltimore, MD, USA

³ Department of Astronomy, University of Massachusetts, Amherst, MA, USA

⁴ Department of Physics and Astronomy, University of Notre Dame, South Bend, IN, USA

⁵ Department of Chemistry and Physics, Saint Michael’s College, Colchester, VT, USA

⁶ Astronomy Department, University of Arizona, Tucson, AZ 85721, USA

⁷ Leiden Observatory, Leiden University, NL-2300 RA Leiden, The Netherlands

⁸ CASA, Department of Astrophysical and Planetary Sciences, University of Colorado, Boulder, CO 80309, USA

⁹ University of the Western Cape, Bellville, Cape Town 7535, South Africa

¹⁰ Department of Astronomy, The Ohio State University, Columbus, OH, USA

Received 2014 March 4; accepted 2014 June 21; published 2014 August 8

ABSTRACT

We analyze the physical conditions of the cool, photoionized ($T \sim 10^4$ K) circumgalactic medium (CGM) using the COS-Halos suite of gas column density measurements for 44 gaseous halos within 160 kpc of $L \sim L^*$ galaxies at $z \sim 0.2$. These data are well described by simple photoionization models, with the gas highly ionized ($n_{\text{H II}}/n_{\text{H}} \gtrsim 99\%$) by the extragalactic ultraviolet background. Scaling by estimates for the virial radius, R_{vir} , we show that the ionization state (tracked by the dimensionless ionization parameter, U) increases with distance from the host galaxy. The ionization parameters imply a decreasing volume density profile $n_{\text{H}} = (10^{-4.2 \pm 0.25})(R/R_{\text{vir}})^{-0.8 \pm 0.3}$. Our derived gas volume densities are several orders of magnitude lower than predictions from standard two-phase models with a cool medium in pressure equilibrium with a hot, coronal medium expected in virialized halos at this mass scale. Applying the ionization corrections to the H I column densities, we estimate a lower limit to the cool gas mass $M_{\text{CGM}}^{\text{cool}} > 6.5 \times 10^{10} M_{\odot}$ for the volume within $R < R_{\text{vir}}$. Allowing for an additional warm-hot, O VI-traced phase, the CGM accounts for *at least* half of the baryons purported to be missing from dark matter halos at the $10^{12} M_{\odot}$ scale.

Key words: galaxies: formation – galaxies: halos – intergalactic medium – quasars: absorption lines

Online-only material: color figures, figure set

1. INTRODUCTION

Baryons account for 17% of the gravitating mass in the universe ($\Omega_b = 0.17 \Omega_m$; Blumenthal et al. 1984; Dunkley et al. 2009). Yet, observational inventories reveal a shortage of baryons on both universal and galaxy-halo scales. The first “missing baryon problem” is illustrated by counting all the baryons revealed by observations of stars, dust, and gas in galaxies and clusters (Ω_g). The total is significantly less than the value expected from the widely accepted big bang nucleosynthesis model, weighing in at only $0.03\text{--}0.07\Omega_b$ (Persic & Salucci 1992; Fukugita et al. 1998; Bell et al. 2003). Second, baryons are apparently missing from galaxies themselves in what is known as the galaxy halo missing baryon problem (McGaugh 2008; Bregman & Lloyd-Davies 2007; McGaugh et al. 2010). To explain these baryon shortages, one must invoke unseen or poorly defined components: highly photoionized intergalactic hydrogen, known as the Ly α forest (Lynds 1971; Sargent et al. 1980; Cen et al. 1994), the warm-hot intergalactic medium, or WHIM (Cen & Ostriker 1999; Davé et al. 1999), and the circumgalactic medium, or CGM (e.g., Bergeron 1986; Lanzetta et al. 1995). In cosmological hydrodynamical simulations, for instance, baryons are apportioned comparably between the Ly α forest (40%), the CGM (25%), and the WHIM (25%, excluding the gas that is also CGM; Davé et al. 2010).

The present work concerns the halo missing baryon problem, which we briefly summarize here. Generally speaking, the condensed baryonic component of galaxies, which dominates the energy output of the system, is predicted to dynamically trace the underlying dark matter halo. Traditionally, baryon counting in this regime has focused on a galaxy’s stars, cold interstellar medium (ISM), and its hot X-ray halo gas (Bell et al. 2003; Klypin et al. 2011; Baldry et al. 2008; Yang et al. 2009; McGaugh et al. 2010; Anderson & Bregman 2010; Papastergis et al. 2012; Gupta et al. 2012). Compared to the cosmological Ω_b/Ω_m ratio, galaxies and their halos come up significantly short on baryons. For a Milky-Way-luminosity galaxy, the various estimates of the ratio in stellar mass to the dark matter mass within the virial radius range from $M_*/M_{\text{DM}} \approx 0.02\text{--}0.05$ (Behroozi et al. 2010); when we add the cold, neutral component from H I surveys (Martin et al. 2010), this fraction increases to only 0.07. Finally, when we add in the detected X-ray halo gas, the fraction is at most 0.08 (however, see Gupta et al. 2012; Fang et al. 2013). Such a deficiency is often expressed in terms of $(M_{\text{stars,gas}}/M_{\text{DM}})/(\Omega_b/\Omega_m)$. In this representation, galaxy halos appear to be missing approximately 60% of their baryons, suggesting that they are structures nearly devoid of baryons both in mass and spatial extent.

Models of the formation of galaxies like our Milky Way have long predicted that the central galaxy contains only a modest fraction of the available baryons (Klypin et al. 2011 and references therein). Galaxies are inefficient producers that

¹¹ Hubble Fellow.

have converted a small portion of their available gas into stars. In turn, theorists have suggested a suite of physical processes to suppress star formation and/or expel gas from the galaxies (Dekel & Silk 1986; Somerville & Primack 1999; Oppenheimer et al. 2010). While evidence for outflowing gas from galaxies is common (e.g., Weiner et al. 2009; Rubin et al. 2013), its impact on the efficiency of galaxy formation is unclear. Furthermore, feedback processes are also required to explain the observed incidence of metal line absorption along quasar sightlines (e.g., D’Odorico & Savaglio 1991; Oppenheimer et al. 2012; Booth et al. 2012) and to enrich the CGM of modern galaxies (e.g., Chen et al. 2010b; Prochaska et al. 2011; Tumlinson et al. 2011).

Over the past 20 years it has become increasingly apparent that galaxies also exhibit a diffuse baryonic component within the dark matter halo that extends far from the inner regions to the virial radius and beyond (Morris et al. 1993; Lanzetta et al. 1995; Tripp et al. 1998; Wakker & Savage 2009; Prochaska et al. 2011). This halo gas or CGM is similar in concept to the intracluster medium revealed in X-ray emission, but the CGM is observed via UV absorption lines and has a much lower temperature and density (Werk et al. 2013). As such, much of the CGM cannot be traced with X-ray imaging or any other radiative emission process: it is simply too diffuse to permit direct detection with any present-day telescope.

Our collaboration, COS-Halos, has been working to characterize this elusive multiphase medium (Tumlinson et al. 2011, 2013; Thom et al. 2012; Werk et al. 2012, 2013). We have designed and executed a large program with the Cosmic Origins Spectrograph (COS; Froning & Green 2009; Green et al. 2012) on the *Hubble Space Telescope* (HST) that observed halo gas of 44 galaxies, drawn from the imaging data set of the Sloan Digital Sky Survey (SDSS), whose angular offsets from quasar sightlines and photometric redshifts implied impact parameters ($R < 160$ kpc) well inside their virial radii. These data comprise a carefully selected, statistically sampled map of the physical state and metallicity of the CGM for $L \approx L^*$ galaxies.

Of particular relevance to the halo missing baryon problem is the total baryonic mass contained in the multiphase CGM, as traced by absorption from hydrogen and metal lines in various ionization states (e.g., Mg II, Si II, C II, Si III, C III, Si IV, O VI).¹² Previous studies have attempted to estimate the total mass contribution of the CGM to a typical L^* galaxy with varying degrees of success. Using absorber samples from HST and FUSE (Penton et al. 2004; Tripp et al. 2005, 2008; Danforth et al. 2006; Thom & Chen 2008; Danforth & Shull 2008; Chen & Mulchaey 2009), and ground-based follow-up spectroscopy to determine redshifts of galaxies along the lines of sight, Prochaska et al. (2011) report a strong H I-traced CGM out to 300 kpc for all galaxy types. They estimate a baryonic mass of $10^{10.5 \pm 0.3} M_\odot$ for an assumed constant total hydrogen column, $N_H = 10^{19} \text{ cm}^{-2}$. Tumlinson et al. (2011) determine the minimum mass of the highly ionized CGM ($T \approx 10^{5-5.5} \text{ K}$) as traced by O VI absorption to be $> 10^9 M_\odot$, based on the maximum possible value for the ionization fraction of O VI ($f_{\text{O VI}} < 0.2$; but the fraction may be higher and the corresponding mass lower in some non-equilibrium scenarios;

Vasiliev et al. 2013) and assuming the CGM extends to only 160 kpc.

Based on H I measurements and a simple halo model that uses a power-law gas density profile exposed to a uniform ionizing background, Thom et al. (2012) estimate that the total mass of the CGM could range from 10^9 to $10^{11} M_\odot$. Zhu & Ménard (2013) and Lan et al. (2014) use statistical techniques to assess the absorption from Ca II and Mg II in galaxy halos, and find an order of magnitude more cool gas in the CGM than in the ISM of galaxies, implying a larger total gas mass in the CGM than in the ISM. Stocke et al. (2013) model the ionization state and metallicity of $T \sim 10^4 \text{ K}$ CGM clouds using absorption line data from COS and the Space Telescope Imaging Spectrograph (STIS). They statistically associate late-type galaxies from SDSS imaging with the COS/STIS absorbers using virial radii estimated from photometry. Based on their assumed galaxy/absorber associations, they estimate that the low-ion CGM can account for between 10% and 15% of the total baryonic budget of luminous spiral galaxies. This estimate is a lower limit because of saturated H I absorption lines.

Here, we refine these mass calculations by modeling the photoionized gas of the CGM using a carefully selected sample of $L \approx L^*$ galaxies with precise, accurate redshift measurements from Keck and Magellan spectroscopy (Werk et al. 2012) whose 10^4 K CGM is probed by HST/COS spectroscopy. Our sample covers and detects a large suite of ions (Werk et al. 2013; Tumlinson et al. 2013). We rigorously determine the ionization state and metallicities for 33 of the COS-Halos sightlines that provide the best-determined measurements of H I and metal line column densities. With the constraints imposed by the data and models, we are able to provide a conservative mass estimate for an $L \approx L^*$ galaxy’s CGM, and show that the CGM is a dominant reservoir of baryons on galactic scales.

Section 2 summarizes the sample and data used in our analysis; in Section 3, we discuss the results of the photoionization modeling and tabulate all derived ionization parameters, metallicities, and total hydrogen columns of the individual lines of sight; in Section 4 we present our analysis of these results, including a mass estimate of the photoionized diffuse gas in the CGM of $L \approx L^*$ galaxies; Section 5 presents a discussion of this result in the context of previous mass estimates, cosmological simulations, and simple hydrostatic solutions. We present a summary and conclusions in Section 6. We additionally provide an Appendix that details the photoionization modeling, explores additional sources of ionization, and discusses the results on a sightline-by-sightline basis. To maintain consistency with previous COS-Halos results, throughout this work we assume the five-year WMAP cosmology with $\Omega_\Lambda = 0.74$, $\Omega_m = 0.26$, and $H_0 = 72 \text{ km s}^{-1} \text{ Mpc}^{-1}$ (Dunkley et al. 2009). Distances and galaxy virial radii are given in proper coordinates. We use atomic data for absorption lines from Morton (2003), and the solar relative abundances of metals from Asplund et al. (2009).

2. SAMPLE, OBSERVATIONS, AND MEASUREMENTS

We draw our sample from the COS-Halos survey of the CGM gas surrounding $L \approx L^*$ galaxies in the low-redshift universe. Using the HST/COS, COS-Halos observed 39 UV-bright quasars within an impact parameter $R < 160$ kpc of 44 galaxies with $0.1 L^* < L < 3 L^*$ at $z \sim 0.2$. The primary motivation and the details of the survey design and execution are discussed in detail in Tumlinson et al. (2013). Previous papers describing the COS-Halos sample and data include the Werk

¹² The commonly used temperature-based nomenclature for the CGM gas phases is different from that of the ISM. The circumgalactic gas in the temperature range $10^4 \text{ K} \leq T < 10^5 \text{ K}$ is typically referred to as cool; the gas in the temperature range $10^5 \text{ K} \leq T < 10^7 \text{ K}$ is called warm-hot; and gas above 10^7 K is called hot, and would be observed via X-ray transitions. Each of these gas phases is highly ionized.

et al. (2012) compilation of galaxy spectroscopy, the Tumlinson et al. (2011) study of O VI bimodality in galaxy halos, the Thom et al. (2012) study of H I in early type galaxies, the Werk et al. (2013) empirical description of the CGM as seen in metal absorption lines, and the Peebles et al. (2014) metal census. In this work we use the same 44 galaxy sample described extensively in Werk et al. (2013) and Tumlinson et al. (2013).

For every sightline, COS observations yielded a continuous spectrum spanning $\lambda \approx 1150\text{--}1800\text{ \AA}$. The exposure times were chosen to achieve a signal-to-noise ratio (S/N) of 7–15 per resolution element (FWHM $\approx 15\text{ km s}^{-1}$) at $\lambda \approx 1300\text{ \AA}$. Keck/High Resolution Echelle Spectrograph (HIRES) echelle spectra supplement the far-UV spectra from *HST*/COS for all of the sightlines included in this work. For galaxies at $z > 0.1$, these data provide coverage of the Mg II $\lambda\lambda 2796, 2803$ doublet, an excellent diagnostic of cool ($T \leq 10^4\text{ K}$), metal-enriched gas. Both the COS and HIRES data have been described in the previous works mentioned above, and we do not repeat the details here. We use the column densities of the metal ion lines presented by Werk et al. (2013) which are derived using the apparent optical depth method (Savage & Sembach 1991). Non-detections are given as 2σ upper limits. We use the H I column densities presented by Tumlinson et al. (2013), also based on the AODM calculations, except for damped systems which are based on Voigt profile fits. Of the 44 galaxies considered here, 40 (91%) show H I absorption in the CGM out to 160 kpc with column densities of $15.0\text{ cm}^{-2} < \log N_{\text{H I}} < 20.0\text{ cm}^{-2}$. These values are presented in Table 1, along with additional constraints on the upper and lower limits, as described more thoroughly in the Appendix.

Low and intermediate ionization state metal absorption lines (singly and doubly ionized species) are a common feature of the CGM for L^* galaxies of all spectral types. Of the 44 sightlines in Werk et al. (2013) sample, 33 (75%) show absorption from low/intermediate ionization state material that allow us to model the ionization state of the intervening gas. It is these 33 sightlines that we now analyze in greater detail to constrain the physical conditions of circumgalactic gas, and to provide a reliable baryonic mass estimate for the cool CGM of $z \sim 0$ L^* galaxies. Figure 1 shows the distribution of host galaxy stellar masses for the full COS-Halos sample, and for the sub-sample of sightlines with data that allow for an estimate of the gas ionization parameter. A Kolmogorov-Smirnov (K-S) test indicates no statistically significant difference between the full COS-Halos sample and the CLOUDY-modeled sub sample in terms of stellar mass, or any other galaxy property.

Throughout this work, we scale the projected distance from the sightline to the center of the host galaxy (impact parameter, R) to the virial radius of the galaxy, approximated here as R_{200} , the radius at which the halo mass density is 200 times the critical matter density of the universe. At a given galaxy stellar mass determined by *kcorrect* (Blanton et al. 2003) from the SDSS *ugriz* photometry, we interpolate along the abundance matching relation of Moster et al. (2010) to find the halo mass (M_{halo}). We then compute a virial radius with the relation:

$$R_{200}^3 = 3M_{\text{halo}}/4\pi\Delta_{\text{vir}}\rho_{\text{matter}}, \quad (1)$$

where ρ_{matter} is the critical density at the spectroscopically determined galaxy redshift times Ω_m , and $\Delta_{\text{vir}} = 200$. At the typical redshifts of the COS-Halos galaxies ($z \sim 0.2$), R_{200} is slightly larger than the virial radius by a factor of ~ 1.2 . Systematic errors in the stellar mass estimates and the scatter and uncertainty in the $M_{\text{halo}}\text{--}M_*$ relation gives an uncertainty in

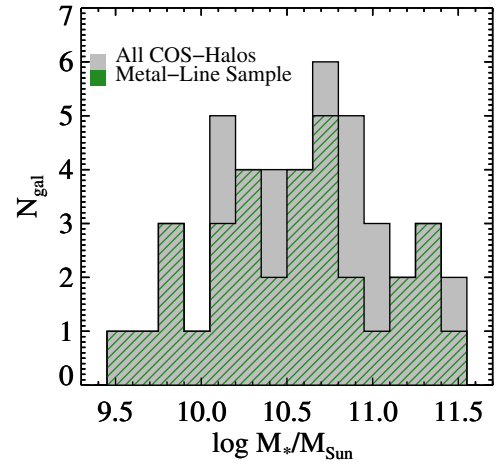


Figure 1. Histogram of stellar masses for the full COS-Halos sample of 44 quasar/galaxy pairs (gray) and the 33 quasar/galaxy pairs that comprise our CLOUDY subsample (green lines), for which we are able to obtain solutions for the ionization parameter of the gas from CLOUDY photoionization modeling of the low ionization state metal absorption lines. The metal line sub-sample spans the full range of stellar masses probed by COS-Halos, with a median value of $10^{10.5} M_{\odot}$, also the stellar mass of the Milky Way.

(A color version of this figure is available in the online journal.)

R_{200} of approximately 50%. Throughout this work we refer to this quantity R_{200} as R_{vir} , as is commonly done.

3. IONIZATION STATE AND METALLICITY OF THE L^* CGM

We model the CGM of 33 COS-Halos galaxies exhibiting absorption from low and intermediate ionization state metals (which we abbreviate here as low-ions and intermediate-ions, respectively) using version 13.03 of CLOUDY (hereafter C13, Ferland et al. 1998, 2013) with the Haardt & Madau (2001, hereafter HM2001) background radiation field from quasars and galaxies (HM2001) as our ionization source for gas. Specifically, we model the individual ionization states of multiple elements for each galaxy halo. For each absorber, we vary the ionization parameter ($\log U$) and the metallicity ($[\text{X}/\text{H}]$; elements are assumed to have solar abundance ratios) to search for CLOUDY models that are consistent with the column densities of the H I and low and intermediate metal ions determined from the observations. We thoroughly discuss the details of each sightline analysis, including systematic uncertainty, in the Appendix. The largest source of error arises from uncertainty in the extragalactic ultra-violet background (EUVB) and other potential sources of ionization (e.g., the galaxy itself; the cosmic ray background). We explore the effects of implementing different slopes and intensities of the background radiation field, including a comparison between Haardt & Madau (2001) and Haardt & Madau (2012), and find the derived ionization parameters and metallicities remain consistent within a few tenths of a dex for a range of physically plausible radiation fields. The uncertainty in the slope of the EUVB therefore lends an additional systematic error of ± 0.3 dex to our derived gas parameters. In the Appendix, we additionally explore the effect of adding ionization from a central star-forming galaxy at various impact parameters from the line of sight.

Four key assumptions underlie our methodology.

1. The low and intermediate ions observed in the COS spectra (e.g., Si II, Si III; C II, C III) arise from a single gas phase with the same origin (i.e., are co-spatial).

Table 1
Derived Physical Parameters

SDSS Field	Galaxy ID	z	R (kpc)	R/R_{vir}	$\log M_*$	Q Flag	$N_{\text{H I}}$ Allowed	$N_{\text{H I}}$ Adopted	$\log U$	[X/H]	$\log N_{\text{H}}$	N_{H} Adopted
J0226+0015	268_22	0.23	78	0.22	10.8	1	14.2 ± 0.03
J0401-0540	67_24	0.22	83	0.35	10.1	5	[15.6, 16.5]	15.6	[-1.8, -1.3]	[-1.2, -0.4]	[19.4, 19.9]	19.7
J0803+4332	306_20	0.25	77	0.11	11.3	2	14.8 ± 0.04	14.8	[-2.8, -1.0]	[-1.7, 0.0]	[17.6, 19.7]	18.7
J0910+1014	34_46	0.14	112	0.34	10.6	3	[15.8, 18.5]	16.5	[-3.5, -2.0]	[-1.3, -0.2]	[18.4, 20.0]	19.1
J0910+1014	242_34	0.26	135	0.16	11.4	4	[16.5, 18.2]	17.0	[-4.0, -3.4]	[-1.8, 0.0]	[18.4, 19.0]	18.7
J0914+2823	41_27	0.24	101	0.51	9.8	3	15.5 ± 0.03	15.5	[-3.1, -1.8]	[-1.4, -0.5]	[17.7, 19.2]	18.5
J0925+4004	196_22	0.25	83	0.12	11.3	3	19.5 ± 0.15	19.6	[-3.8, -3.0]	-0.7 ± 0.2	[20.0, 20.3]	20.1
J0928+6025	110_35	0.15	91	0.24	10.8	4	19.4 ± 0.15	19.5	[-3.6, -2.8]	-0.4 ± 0.2	[19.9, 20.3]	20.1
J0935+0204	15_28	0.26	110	0.26	11.0	1	<12.68
J0943+0531	106_34	0.23	121	0.34	10.8	2	[15.4, 20.0]	15.4	[-3.0, -1.5]	[-1.0, 0.0]	[17.8, 19.5]	18.5
J0943+0531	216_61	0.14	149	0.33	11.0	1	[14.9, 17.0]
J0943+0531	227_19	0.35	92	0.55	9.6	3	16.3 ± 0.03	16.3	[-2.5, -1.0]	-1.6 ± 0.2	[19.4, 21.2]	20.2
J0950+4831	177_27	0.21	91	0.15	11.2	4	[17.5, 18.5]	18.5	[-3.3, -2.7]	[-1.5, 0.0]	[19.8, 20.4]	20.1
J1009+0713	204_17	0.23	60	0.29	9.8	3	[16.0, 18.2]	16.2	[-3.0, -2.0]	[-2.2, 0.0]	[18.5, 19.6]	19.1
J1009+0713	170_9	0.36	44	0.20	10.2	4	[18.0, 18.9]	18.5	[-3.0, -2.5]	-0.6 ± 0.2	[20.0, 20.5]	20.2
J1016+4706	274_6	0.25	23	0.10	10.2	5	[16.6, 18.5]	16.6	[-2.9, -2.7]	<-0.1	[18.9, 19.2]	19.1
J1016+4706	359_16	0.17	44	0.15	10.5	5	[16.4, 18.2]	16.4	[-3.5, -2.9]	<-0.1	[18.1, 18.7]	18.4
J1112+3539	236_14	0.25	53	0.21	10.3	5	[15.8, 17.5]	15.8	[-3.5, -3.0]	<-0.3	[17.6, 18.1]	17.8
J1133+0327	110_5	0.24	18	0.03	11.2	5	18.6 ± 0.06	18.6	[-3.6, -3.3]	-1.0 ± 0.2	[19.5, 19.8]	19.7
J1133+0327	164_21	0.15	55	0.23	10.1	1	[15.8, 18.0]
J1157-0022	230_7	0.16	19	0.05	10.8	1	[15.6, 17.6]
J1220+3853	225_38	0.27	154	0.47	10.7	5	15.8 ± 0.05	15.8	[-2.5, -1.9]	-0.6 ± 0.2	[18.7, 19.4]	19.1
J1233+4758	94_38	0.22	132	0.38	10.8	5	[16.7, 18.3]	16.7	[-3.2, -2.9]	<-0.4	[18.8, 19.1]	18.9
J1233-0031	168_7	0.32	32	0.12	10.5	3	15.6 ± 0.02	15.6	[-2.4, -1.3]	[-1.3, 0.0]	[18.7, 20.0]	19.3
J1241+5721	199_6	0.21	20	0.08	10.2	3	[16.9, 18.5]	17.9	[-3.6, -2.5]	[-1.2, 0.0]	[19.3, 20.4]	19.9
J1241+5721	208_27	0.22	93	0.41	10.0	4	15.3 ± 0.06	15.3	[-3.3, -2.9]	0.0 ± 0.2	[17.2, 17.6]	17.4
J1245+3356	236_36	0.19	112	0.54	9.8	3	14.8 ± 0.04	14.8	[-2.4, -1.3]	[-1.8, -1.1]	[18.1, 19.4]	18.7
J1322+4645	349_11	0.21	37	0.10	10.8	4	[16.3, 18.3]	16.3	[-3.0, -2.2]	[-1.9, -0.3]	[18.5, 19.4]	19.0
J1330+2813	289_28	0.19	87	0.33	10.3	4	[16.5, 18.5]	16.6	[-3.7, -2.7]	<-0.2	[18.2, 19.2]	18.7
J1342-0053	157_10	0.23	35	0.09	10.9	5	[18.3, 19.5]	19.0	[-3.5, -3.0]	[-0.5, 0.0]	[19.7, 20.0]	19.8
J1342-0053	77_10	0.20	32	0.11	10.5	1	<12.43
J1419+4207	132_30	0.18	88	0.28	10.6	2	[15.4, 18.1]	17.0	[-4.3, -3.3]	[-1.9, 0.0]	[18.1, 19.0]	18.5
J1435+3604	126_21	0.26	83	0.32	10.4	4	15.3 ± 0.06	15.3	[-3.0, -2.5]	-0.4 ± 0.2	[17.6, 18.2]	17.8
J1435+3604	68_12	0.20	39	0.08	11.1	5	19.8 ± 0.10	19.8	[-3.6, -3.0]	-1.2 ± 0.2	[20.2, 20.4]	20.3
J1437+5045	317_38	0.25	143	0.62	10.1	1	14.5 ± 0.12
J1445+3428	232_33	0.22	113	0.42	10.4	1	15.1 ± 0.06
J1514+3619	287_14	0.21	47	0.24	9.7	4	[16.5, 18.4]	16.5	[-4.0, -3.0]	<-0.5	[17.9, 18.9]	18.3
J1550+4001	197_23	0.31	102	0.15	11.3	5	16.5 ± 0.03	16.5	[-3.0, -2.5]	-0.8 ± 0.2	[18.9, 19.5]	19.1
J1550+4001	97_33	0.32	150	0.41	10.9	1	13.9 ± 0.09
J1555+3628	88_11	0.19	34	0.11	10.5	4	[16.8, 18.3]	17.2	[-3.5, -2.6]	[-1.6, 0.0]	[19.1, 20.0]	19.6
J1617+0638	253_39	0.15	101	0.09	11.5	1	<13.12
J1619+3342	113_40	0.14	97	0.39	10.1	4	[15.0, 17.5]	15.0	[-2.4, -1.6]	<-0.1	[17.9, 18.8]	18.4
J2257+1340	270_40	0.18	116	0.28	10.9	1	<12.53
J2345-0059	356_12	0.25	46	0.13	10.8	4	16.0 ± 0.04	16.0	[-2.6, -2.2]	-0.3 ± 0.2	[18.7, 19.2]	19.0

Notes. (1) SDSS field identifier and (2) galaxy identifier, given as P.A. ($^\circ$) and angular separation ($''$) from the QSO, respectively. (3) Spectroscopic redshift (Werk et al. 2012). (4) Projected separation in kiloparsecs, calculated in the galaxy restframe. (5) Projected separation scaled to the virial radius of the galaxy. (6) Log stellar mass from *kcorrect* (Blanton et al. 2003). (7) Quality flag; 1–5 (low to high) where absorbers having $Q > 2$ are included in the analysis. (8) Range of $\log N_{\text{H I}}$ allowed by COS data. (9) Adopted H I column density. (10) Range of $\log U$ allowed by data. (11) Range (or estimate) of [X/H]. (12) Range of total hydrogen column density ($\log \text{cm}^{-2}$): low value is based on AODM H I column density and lowest $\log U$; high value is from adopted H I column density and highest allowed $\log U$. (13) Log of the adopted total hydrogen column, calculated using the adopted H I column density and the mean $\log U$ for each sightline.

2. The CGM probed by this absorption is a cool medium, i.e., $T < 10^5$ K, in which photoionization dominates.
3. The absorption from the low and intermediate ions trace the majority of observed H I gas.
4. The gas is in ionization equilibrium.

None of these assumptions is radical—all four are now standard practice in analyses of quasar absorption-line spectra probing both the CGM and intergalactic medium (IGM; e.g., Prochaska et al. 2004). With respect to the first assumption, Werk et al. (2013) has shown that the kinematic component structure of

the low-ion and intermediate-ion absorption profiles is similar. Generally, the intermediate-ion absorption tends to be stronger than the low-ion absorption in the CGM of L^* galaxies, but there is no evidence that the low and intermediate ionic absorption arise from different gas phases based on their component structure alone. Second, our observations of low-ion transitions in the majority of the spectra considered here demands that the gas be cool ($T < 10^5$ K). Tumlinson et al. (2013) have further demonstrated this temperature constraint based on the H I line widths. Collisional ionization of gas at $T > 10^{4.6}$ K would yield negligible quantities of ions like Mg II, C II, and Si II, even if at

solar abundance and with a large total gas column (e.g., Gnat & Sternberg 2007). Furthermore, the nine galaxies that exhibit only intermediate ions (C III, Si III) are constrained to have $T < 2 \times 10^5$ K to avoid extremely large gas surface densities. Put another way, this assumption of a cool medium is conservative with regard to a total mass estimate. Finally, these low- and intermediate-ion metals trace the majority of observed H I gas, as evidenced by both their line profiles and the observed trend between $N_{\text{H I}}$ and metal column density shown by Werk et al. (2013).

To reduce systematics arising from different ionization processes, we have not attempted to model the O VI detected in these systems (Tumlinson et al. 2011). O VI is potentially produced by multiple ionization processes (i.e., photoionization and collisional ionization), and modeling the amount of gas from these two physically distinct origins is complex and beyond the scope of this paper. Recent simulations by Ford et al. (2013) predict that while absorption from low-ions in the CGM of $L \approx L^*$ galaxies arises from denser gas closer to galaxies, higher ions like O VI trace hotter, more diffuse gas extending to larger radial distances. Similarly, Stinson et al. (2012) find that their MaGICC halos display two distinct phases: a cool, $T \approx 10^4$ K dense gas that follows the H I absorption, and a warm-hot $T > 10^5$ K low-density medium that creates the O VI absorption primarily through collisional ionization. Observationally, Fox et al. (2013) have shown that O VI absorption exhibits a significantly higher velocity spread than C II, and conclude that low-ions and high-ions trace distinct gas phases in Lyman limit systems. Even when the low-ions and high-ions are kinematically very similar, several recent studies have shown that the observed column densities of low- and high-ionization species cannot be reproduced with a single gas phase (e.g., Tripp et al. 2011; Meiring et al. 2013; Lehner et al. 2013).

Thus, our mass estimate explicitly excludes gas in a highly ionized O VI phase which may itself comprise a large component of the CGM (Tumlinson et al. 2011). As shown in the Appendix, our best models for each system tend to systematically underestimate the column density of the O VI absorption, which reinforces the conclusions reached in the studies above with a larger and more statistically uniform sample. That is, when we detect O VI in our COS observations, its typical ionic column density requires an ionization parameter between 1 and 2 dex higher than the solution for the lower ionization state lines. Typically, O VI requires $\log U > -1.5$ if it is primarily photoionized. One caveat is that it may be possible to produce more O VI by considering ionizing photons from a nearby, central starburst galaxy, including X-ray binaries, as has recently been shown by Vasiliev et al. (2013). The O VI fraction can reach 60% (compared to 20% from photoionization) over a wide temperature range when superimposing on HM2001 a time-dependent radiation field of a nearby starburst galaxy with soft X-rays. We note that in this case, the ionization parameters required to simultaneously reproduce the low-ions are much higher than those we derive using a HM2001 spectrum alone, which further serves to make our mass estimate of the $\sim 10^4$ K CGM a lower limit. Finally, we also do not consider the time-dependent, non-equilibrium ionization models of Oppenheimer & Schaye (2013) for O VI, where an active galactic nucleus (AGN) in the recent past photoionized metals with a significantly stronger field than that of HM2001. They predict that the amount of O VI can increase by at least 1 dex, if, for example, a COS-Halos galaxy was a Seyfert within the last 10 Myr and has since turned off. For reference, none of the members of the COS-Halos galaxy sample are defined as AGN

according to the Baldwin, Phillips, & Terlevich (BPT) diagram, and we expect that this non-equilibrium fluctuating scenario is not relevant for these galaxies.

We consider Si IV to the extent that it can provide an upper bound on the ionization parameter of the gas.¹³ For example, the photoionization models predict a column density of Si IV depending on $\log U$, and we require that the Si IV data must lie at or above this level. Typically, we can explain the majority of the Si IV absorption with the photoionization modeling, and our models match the Si IV column densities (or limits) well.

In the 19 (of 33) cases for which the Lyman series absorption lines exhibit saturated profiles, we assume the lowest possible value of the H I column density. In 7 of these 19 cases, we are forced to assume $N_{\text{H I}}$ slightly higher than the AODM lower limit in order to determine a self-consistent solution with CLOUDY. We discuss these details in the Appendix. The best-fitting value of $[X/H]$ is highly dependent on the assumed $\log N_{\text{H I}}$, and thus we cannot reliably determine the gas metallicity in cases hampered by H I lower limits. For this reason, we generally find upper limits to the metallicity. The ionization parameter, as discussed in the Appendix, is largely immune to uncertainty in the H I column density. This is because we can independently constrain $\log U$ from the CLOUDY models based on several different ionization states of the same metal line, and the detection of a number of different metal lines of various ionization states (e.g., C II, C III, Si II, Si III, Si IV, N II, N III, Mg II). Our choice to adopt the minimum $N_{\text{H I}}$ consistent with the data leads to a conservatively low total N_{H} and minimizes the implied mass in some cases by as much as an order of magnitude.

For each of the 33 galaxy absorbers included in this analysis, we detail the specific ions used in the solution for $\log U$ and $[X/H]$ and the overall consistency, accuracy, and precision of this solution in the Appendix. In all cases, we provide a range of $\log U$, gas volume density, and $[X/H]$ allowed by the data, along with the corresponding allowed range of the total hydrogen column (photoionized + neutral) along each line of sight. Galaxy properties are given in conjunction with constraints on the metallicity, total gas column density, and ionization state of their CGM in Table 1.

We have assessed the quality of the solution by visual inspection, parameterized by the quantity “Q flag,” which ranges from 1 to 5 (null solution to well-constrained). This Q flag is based on a combination of an overall data-quality assessment, number and quality of detections of low and intermediate ions, the constraints on the H I column density, and the overall consistency of the solution for the multiple ions and metals. Sightlines that show no absorption from any metal ion are immediately assigned a Q flag of 1 (11 of 44 galaxies). All of these excluded galaxies lie in the optically thin regime. We explore the extent to which excluding them may bias our results for the mass determination of the halos of $L \sim L^*$ galaxies in Section 3.3, and conclude that it could have a modest impact at most. A Q flag of 2 indicates that both $\log U$ and $N_{\text{H I}}$ are poorly constrained by the data, owing to limited detections of metal ions (or many blends) and saturated H I (three galaxies). Generally, a Q flag of 3 signifies that either $\log U$ or $N_{\text{H I}}$ is moderately constrained by the data and modeling, resulting in a range of allowed total hydrogen column that spans approximately 1 dex (eight galaxies). A typical galaxy that is rated with a

¹³ Additionally, in one case, C IV, though for the majority of systems we do not have spectral coverage of the C IV lines at 1548 and 1550 Å.

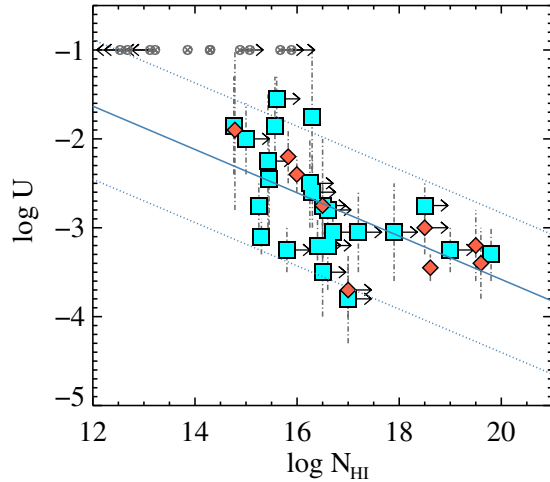


Figure 2. Derived ionization parameter from the CLOUDY modeling vs. H I column density for 44 COS-Halos absorbers within 160 kpc of an $L \sim L^*$ galaxy. The absorbers with star-forming host galaxies are shown as blue squares, while absorbers with host galaxies without any detectable ongoing star formation are shown as red diamonds. The 11 sightlines on which we are able to place no constraints owing to non-detections of all metal ions are shown as gray circled \times 's at an arbitrary $\log U$ of -1 . Upper and lower limits on the measured H I column densities from the COS data are shown, respectively, by left-facing and right-facing arrows. The range of allowed $\log U$ values for each absorber are shown by vertical dash-dotted gray lines. We have fit a line in log-log space to these data points (shown in blue) using a linear regression analysis for 1000 trials with the $\log U$ values randomly distributed along the range of allowed $\log U$ values. We reject the null hypothesis with a probability of 99.994%, and therefore find a correlation between $\log U$ and $\log N_{\text{HI}}$ with 4σ significance.

(A color version of this figure is available in the online journal.)

Q flag of 4 shows saturated H I with a lower limit $>10^{16} \text{ cm}^{-2}$, and good-quality detections from various low and intermediate ions that constrain the solution from $\log U$ to better than 1 dex (12 galaxies). Finally, we reserve our highest Q flag of 5 for solutions that are well-bounded in metallicity and $\log U$ (on average, ± 0.2 dex) and consistent with a suite of column density measurements of several low- and intermediate-ions (9 galaxies). Absorbers with Q flags greater than or equal to 2 are included in the analysis and the systematic uncertainties are discussed in detail in the [Appendix](#).

3.1. Ionization Trends with Gas Column Density and Impact Parameter

The dimensionless ionization parameter, U , is defined as the ionizing photon density divided by the total hydrogen number density (neutral + ionized). For our purposes we explore models with $\log U$ ranging between -1 and -5 , with higher values corresponding to a higher ionized gas fraction and a lower gas density. We derive a mean $\log U$ of -2.8 for our sample of 33 absorbers, which corresponds to approximately 99% of the hydrogen being ionized, on average. Our adopted values of $\log U$ range from -3.8 to -1.6 , corresponding to a range in the neutral gas fraction between approximately 25% and 0.01%. Figure 2 shows $\log U$ versus the H I column density for 44 COS-Halos absorbers within 160 kpc of an $L \sim L^*$ galaxy, with the 11 galaxies excluded from our analysis shown for reference as gray \times 's at an arbitrarily chosen value of $\log U = -1$. Upper and lower limits on the measured H I column densities from the COS data are shown, respectively, by left-facing and right-facing arrows. The colored data points (blue = star-forming; red = non-star-forming) for the 33 lines of sight with metal line data show a clear trend of decreasing ionization parameter with

increasing H I column density. Lehner et al. (2013) carried out a similar CLOUDY-based analysis for Lyman limit systems with $\log N_{\text{HI}} > 16.0$, and found a mean $\log U$ of -3.3 ± 0.6 . When we consider our absorption line systems at similar H I column densities, we also find a mean $\log U$ of -3.3 .

To assess the strength of the correlation between $\log U$ and H I column density, we perform a statistical analysis using the ASURV software package Rev 1.2 (LaValley et al. 1992), which implements the methods presented in Feigelson & Nelson (1985), and Isobe et al. (1986). We include censored data points (i.e., lower limits) in the H I column density. We implicitly assume that the limits are random with respect to the galaxies. Given the range of impact parameters sampled and that the quasars were selected without any knowledge of the absorption, this assumption should hold. We exclude the 11 galaxies with no H I and/or metal-line detections from this analysis, since those data points exhibit censoring in H I column density and $\log U$, which would make any fit unconstrained. We reject the null hypothesis with a probability of 99.994% by performing a Kendall Tau test of censored bivariate data in this parameter space. Thus, $\log U$ and $\log N_{\text{HI}}$ are very likely anti-correlated. To derive the best linear fit to the observed correlation, we perform a linear regression analysis for 1000 trials with the $\log U$ values randomly distributed along the range of allowed $\log U$ values for each absorber (shown by the gray lines in Figure 2). The best-fit, which includes H I column density lower limits, is shown as a solid blue line, and is given by:

$$\log U = (-0.24 \pm 0.06) \log N_{\text{HI}} + (1.3 \pm 0.5). \quad (2)$$

The dotted lines show 1σ confidence intervals of the fit, and the standard error of the regression is 0.38.

Interestingly, this anti-correlation between $\log U$ and $\log N_{\text{HI}}$ is qualitatively consistent with predictions for photoionized clouds in (or not far from) local hydrostatic equilibrium. Schaye (2001) argues that over-dense absorbers, such as those we may observe in the CGM, have sizes of the order of the local Jeans length, regardless of whether the cloud as a whole is in hydrostatic equilibrium. A relation between neutral hydrogen column density and the characteristic volume density naturally arises from this requirement (Equation (8) of Schaye 2001) such that as N_{HI} increases, n_{H} also increases (equivalently, $\log U$ decreases; see also Prochaska et al. 2004). We explore several hydrostatic solutions in Section 5.3.

To compare $\log U$ to the low ionization state metal line absorption, we derive the quantity N_{Low} for each system, defined as follows (Werk et al. 2013): (1) $N_{\text{Low}} = N_{\text{Si II}}$, if the Si II measurement is a value or lower limit; (2) $N_{\text{Low}} = N_{\text{Mg II}}$ if the Si II measurement is an upper limit (or there is none recorded) and an Mg II measurement exists. We choose Si II as the primary low ion because it has multiple transitions in the far-UV bandpass with a range of oscillator strengths yielding more reliable column density estimates. The Mg II doublet, meanwhile, offers more sensitive upper limits. Because we measure $N_{\text{Si II}} \approx N_{\text{Mg II}}$ in cases where both are measured, we apply no offset when adopting one versus the other. In all, there are roughly half of the systems in each category. Figure 3 shows $\log U$ versus N_{Low} for our sample, and bears a high degree of similarity to Figure 2 such that higher values of N_{Low} exhibit lower values of $\log U$. Werk et al. (2013) have shown that N_{Low} is significantly coupled to H I column density, with low-ion detections essentially requiring a non-negligible opacity at the H I Lyman limit. Together, Figures 2 and 3 show that this observed trend follows from the ionization parameter of the

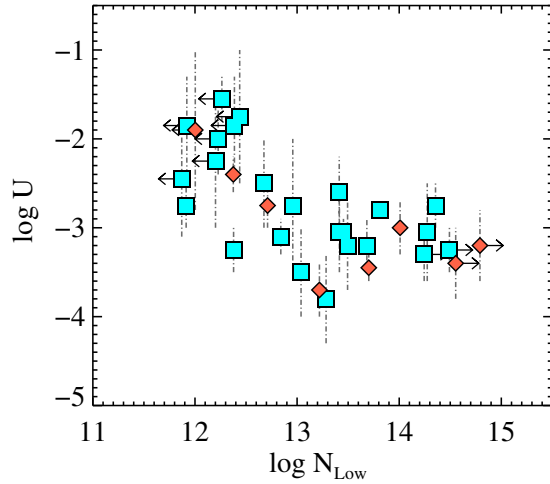


Figure 3. Derived ionization parameter from the CLOUDY modeling vs. low-ion column density for 33 COS-Halos absorbers, where N_{Low} is measured by either Mg II or Si II, as described in Section 3.1.

(A color version of this figure is available in the online journal.)

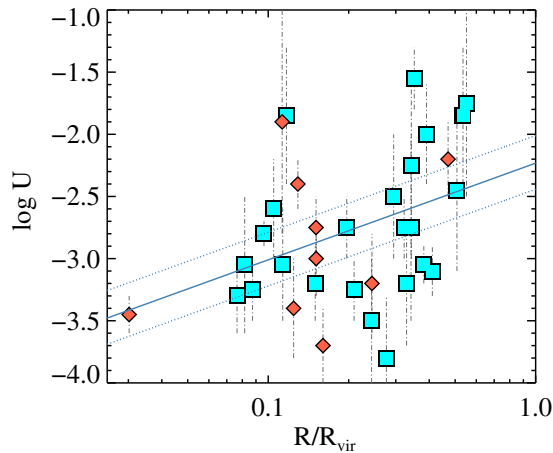


Figure 4. Ionization parameter as $\log U$ vs. impact parameter in units of R/R_{vir} for 33 COS-Halos absorbers within 160 kpc of an $L \sim L^*$ galaxy. The absorbers with star-forming host galaxies are shown as blue squares, while absorbers having host galaxies without any detectable ongoing star formation are shown as red diamonds. The ranges of allowed $\log U$ are shown by the vertical dash-dotted gray lines. We determine the mean $\log U$ by populating a random distribution of allowed $\log U$ 1000 times. The mean $\log U$ of the CGM of $L \sim L^*$ galaxies to 160 kpc is -2.8 . We reject the null hypothesis at 97%, indicating that $\log U$ and impact parameter are correlated. The best-fitting power law slope is $U \propto (R/R_{\text{vir}})^{0.8 \pm 0.3}$.

(A color version of this figure is available in the online journal.)

gas being higher at lower low-ion and H I column densities. We explore the physical significance of this correlation in Section 5.

Figure 4 shows $\log U$ versus R/R_{vir} for the same sample. Despite the large scatter, Figure 4 shows that ionization parameter and impact parameter are positively correlated. A Kendall-Tau test of 1000 trials with the $\log U$ values randomly distributed along the range of allowed values rejects the null hypothesis with a probability of 97%, indicating a positive correlation is present. Based on a linear regression analysis (as implemented in ASURV), we find that the best power-law fit to this correlation is:

$$U = 0.006 \pm 0.003 (R/R_{\text{vir}})^{0.8 \pm 0.3} \quad (3)$$

with a combined standard deviation of ~ 0.5 (shown in blue, with 1σ confidence intervals shown). Thus, the CGM is more highly

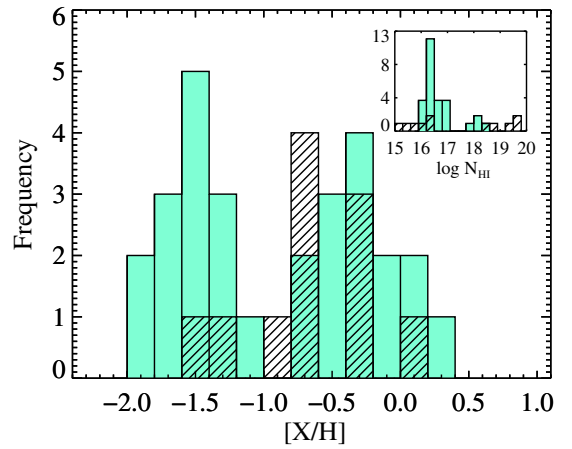


Figure 5. Histogram of CLOUDY-derived metallicities for the Lyman limit systems analyzed by Lehner et al. (2013; light green) and for the 11 COS-Halos absorbers that provide a constraint on the metallicity to better than 0.2 dex (diagonal black lines). An inset in the upper right corner of this plot shows the H I column densities of the Lehner sample (light green) and the sample of COS-Halos absorbers included here (black diagonal). Most of this COS-Halos 11 absorber subsample extends to lower or higher H I column than the Lehner H I column densities and would not have been included in their analysis. While Lehner et al. find evidence of a bimodal distribution of CGM gas metallicity, we do not see evidence for bimodality here though we are limited by a small sample.

(A color version of this figure is available in the online journal.)

ionized farther from its host galaxy. We discuss the extent to which this trend is the result of a declining gas density gradient, in Section 4.1.

3.2. Limited Constraints on the Metallicity of the L^* CGM

As described throughout this work and in detail in the Appendix, our constraints on the gas metallicity are generally poor owing to the line saturation of H I Ly α and other Lyman series lines in our COS data. Nonetheless, for 11 COS-Halos absorbers with well-constrained H I column densities, we are able to estimate the gas metallicity to better than ± 0.2 dex. Our values of $[X/H]$ range from -1.5 to solar, and are determined for galaxies with either $\log N_{\text{HI}} < 16.5 \text{ cm}^{-2}$ where Lyman series lines do not saturate in our COS data or $\log N_{\text{HI}} > 18.5$ where the presence of damping wings on Lyman series absorption lines allows for an estimate of the H I column density from Voigt profile fits (Tumlinson et al. 2013). The 11 systems that do not show absorption from metal ions do not offer any useful upper limits on the gas metallicity. We discuss the limited constraints implied by metal line non-detections more fully in the next section.

Figure 5 compares our gas metallicity for the CGM of L^* galaxies within 160 kpc to the values of Lehner et al. (2013), who analyzed 28 Lyman limit systems and found a bimodal metallicity distribution. We note that the Lehner et al. study examines a range of H I column density where constraints from COS-Halos are the weakest ($16.2 < \log N_{\text{HI}} < 18.5$). A key difference between this study and that of Lehner et al. (2013) is that the COS-Halos target selection is based on galaxy properties, while the Lehner et al. (2013) target selection is based on H I column density selection that allows them to sensitively probe both high and low metallicities. The range of gas metallicities we find is similar to that of the Lyman limit systems examined by Lehner et al. (2013), but we do not have enough data to distinguish any bimodality in metallicity for COS-Halos galaxies. Moreover, we have not analyzed the 11

cases in which no metals are apparent ($Q = 1$), and it is possible some of those cases would occupy the low-metallicity branch.

With respect to a metallicity gradient with R , we find no apparent trend between metallicity and impact parameter for the 33 COS-Halos absorbers included in this analysis, albeit very large uncertainties and upper limits. We have performed a survival analysis in this parameter space using the ASURV to test for any hint of a correlation. A Kendall-Tau test, which includes censoring (upper limits) and 1000 trials with the $[X/H]$ values lying along a randomly populated distribution defined by the range of allowed values, reveals a z -value of 0.689 and rejects the null hypothesis with a probability of only 41%. Because the gas metallicity is poorly constrained by our data, we see no evidence of a metallicity gradient with an impact parameter. The best fitting power-law slope is $[X/H] \propto (R/R_{\text{vir}})^{0.2 \pm 0.4}$. We explore whether this finding is consistent with theoretical predictions from a primarily wind-fed CGM and with naive expectations based on several possible origins of the CGM in Section 5.

3.3. Constraints from Non-detections of Metal Ions

For 7 of the 44 sightlines considered, we have not detected absorption lines other than H I Ly α or Ly β . Four additional galaxy-halo sightlines are devoid of absorption from any ion, including H I Ly α . In this section, we address whether these “undetected” systems are more likely to exhibit low metallicity and/or low N_{H} compared to the sample of 33 absorbers for which we can model the gas using CLOUDY. To do this, we examine the typical upper limits to the column densities of several common metal ions in the parameter space of metallicity and N_{H} . We show that the seven sightlines with H I absorption but no metal absorption can exhibit the full range of physical conditions (ionization parameters, metallicities) for the gas that shows detected metal-ion absorption.

In Figure 6, we plot CLOUDY-derived gas metallicities as a function of the total hydrogen column for the 33 systems showing H I and metal lines. The sizes of the data points are inversely proportional to the errors in their derived quantities, such that larger data points have well-constrained ionization parameters, H I column densities, and/or metallicity. Upper limits to metallicity and lower limits to the total hydrogen column density are shown as diagonal arrows to the bottom right, as the two quantities are degenerate. The filled gray region of this plot showcases the region of this parameter space that is *ruled out* by the typical 2σ upper limits to the Si III column density. These six limits have all been scaled to $\log N_{\text{H I}} = 15.0$ to show in this parameter space. Si III is the most commonly detected metal ion with the best coverage in the COS-Halos data set, and in six of the seven non-detections we can place reliable upper limits on its column density. By comparison, non-detections of the lower ionization state metal ions (e.g., Mg II, Si II, and C II) are completely consistent with the full range of parameter space shown. Other intermediate-ion non-detections, such as N III and C III, are only informative in one and two cases of non-detections. We show the constraints of those upper limits as solid lines of red and blue for C III and N II, respectively. The regions not allowed by these two limiting cases would lie above the plotted curves. Next to the ion name we give the number of 2σ upper limits (out of seven possible) that were averaged.

Figure 6 shows that the allowed metallicities and N_{H} values (i.e., unshaded area) for the “undetected” systems are largely consistent with the ranges exhibited by the 33 data points from the “detected” systems. Thus, there is no reason to assign them

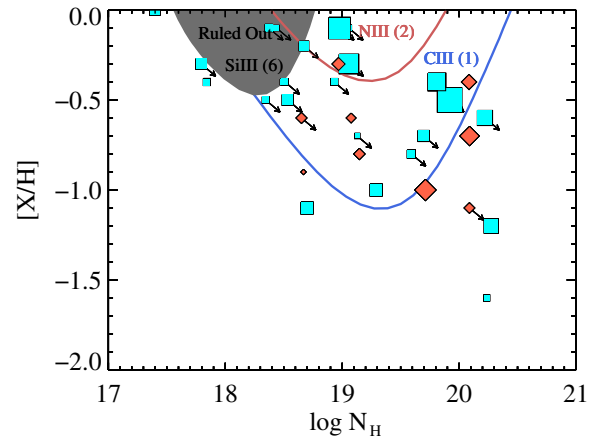


Figure 6. Metallicity vs. total hydrogen column density for the detected sightlines (blue squares = star-forming galaxies; red diamonds = non-star-forming galaxies). The size of each point is inversely proportional to the uncertainty in each quantity. The filled gray region highlights the region of parameter space that is ruled out for the six non-detections in Si III. Additional constraints placed on total hydrogen column and gas metallicity by the 2σ upper limits of other undetected intermediate ions (N III, red and C III, blue) are based on CLOUDY grid lines at $\log N_{\text{H I}} = 15$. The number of undetected systems on which the 2σ upper limit is based is given next to the ion name in each region. While C III is the most constraining of the ions in assessing the state of the gas for this undetected sample, its upper limit is based on only one absorber with H I for which we did not detect C III. The other six absorbers in this sample do not cover the line at 977 Å. Four additional systems show no metal ion absorption and no detection of H I, which we cannot include in this figure.

(A color version of this figure is available in the online journal.)

unusual N_{H} . In general, the 11 systems excluded from this analysis have low H I column densities, $\log N_{\text{H I}} < 15.0$. Based on the relation derived in Section 3.1, we might expect the optically thin gas along these sightlines to have a $\log U \approx -2$, and thus a total hydrogen column density of $\log N_{\text{H}} \approx 10^{19} \text{ cm}^{-2}$. At this value of N_{H} , the upper limits to the column densities of intermediate ionization state lines for 6/7 of the “undetected” systems are consistent with the full range of metallicity considered, from 0.01 solar to solar. As shown, there is one case where the upper limit on C III can rule out a gas total hydrogen column and metallicity that most commonly describes our sample ($[X/H] = -0.5$; $\log N_{\text{H}} = 19.6$ —area above the blue contour). In other words, this sightline requires the assumption of a low gas metallicity ($[X/H] < -1.0$) if the total hydrogen column of the gas is near the median of the detected sample ($\log N_{\text{H}} = 19.6 \text{ cm}^{-2}$).

Other than this one upper limit to $N_{\text{C III}}$, the metal ion non-detections can easily exhibit the same metallicity and total hydrogen column density as the gas we do detect. However, the inverse is also true. The 11 systems for which we detect no metal ion absorption can also exhibit lower gas metallicity and/or lower N_{H} . Essentially, we cannot draw any conclusions about the physical conditions of the gas (or lack thereof) for the 11 “undetected” systems. Hence, we do not have a compelling reason to believe we are biasing our results one way or the other by simply excluding them from our analysis.

4. RESULTS

The COS-Halos survey design and multi-wavelength, high-quality, spectroscopic data set have allowed us to empirically characterize the CGM of L^* galaxies with unprecedented accuracy (Werk et al. 2013; Thom et al. 2012; Tumlinson et al. 2011, 2013; Battisti et al. 2012). With the ionization

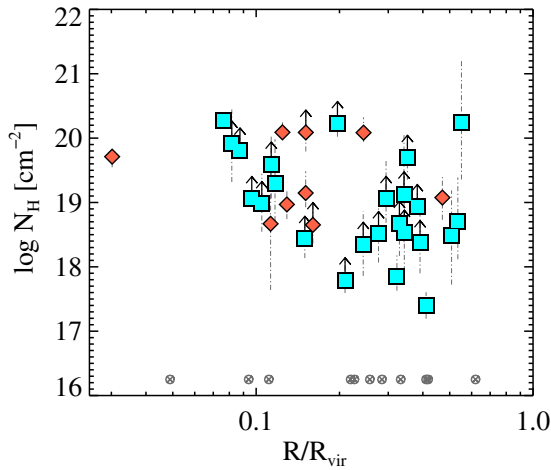


Figure 7. Total hydrogen column from the CLOUDY modeling vs. impact parameter in units of R/R_{vir} for 44 COS-Halos absorbers within 160 kpc of an $L \sim L^*$ galaxy. The absorbers with star-forming host galaxies are shown as blue squares, while absorbers having host galaxies without any detectable ongoing star formation are shown as red diamonds. The 11 sightlines on which we are unable to place constraints (owing to non-detections of all metal ions) are shown as gray circled \times 's at an arbitrarily low $\log N_{\text{H}}$ of 17.2 for reference. We show the absorbers with lower limits to the H I column density with upward-facing arrows. The range of allowed total hydrogen columns at the adopted H I column densities are shown by the vertical dash-dotted gray lines. The mean $\log N_{\text{H}}$ of the CGM of $L \sim L^*$ galaxies calculated including censored data points is 19.6. (A color version of this figure is available in the online journal.)

modeling, we can now characterize the physical nature of the CGM without any additional model-based assumptions regarding, for example, its origin or underlying density profile. In this section, we describe the gas surface and volume density profiles implied by the ionization modeling and absorption-line data. We then use these density profiles to estimate the total amount of photoionized material in the CGM of L^* galaxies. Given that 19 of 33 sightlines show saturated H I absorption lines, and the total hydrogen column scales roughly linearly with the neutral hydrogen column density, our derived CGM mass is a lower limit. However, this lower limit is more constraining than previous values as a result of our detailed CLOUDY analysis that establishes the ionization state of the gas. Previous estimates using the COS-Halos sample (e.g., Tumlinson et al. 2011; Werk et al. 2013) have simply assumed the lowest possible ionized gas fraction in the presence of ionizing radiation from background quasars and galaxies at the characteristic temperatures of prominent ionization species. Other estimates using different samples have employed photoionization modeling (e.g., Lehner et al. 2013; Stocke et al. 2013), and require different sets of assumptions. In the case of the Lehner et al. (2013) study, the sample was selected on H I absorption, and so they must assume a total volume. In the case of Stocke et al. (2013), the sample is partially blind with respect to absorption as COS-Halos, and partially comprised of a “serendipitous” sample of absorbers for which the properties of the host galaxies are less homogeneous than the COS-Halos galaxies.

4.1. Surface and Volume Density Profiles

The total hydrogen column density, N_{H} , is simply the sum of the neutral and ionized hydrogen column densities, where we determine the ionized hydrogen column density directly from the derived ionization parameter of the gas. Thus, $N_{\text{H}} = N_{\text{H I}} + N_{\text{H I}}/(1-\chi)$, where χ is the ionized gas fraction (mean $\approx 99\%$). Table 1 lists both the range of allowed N_{H} and the adopted

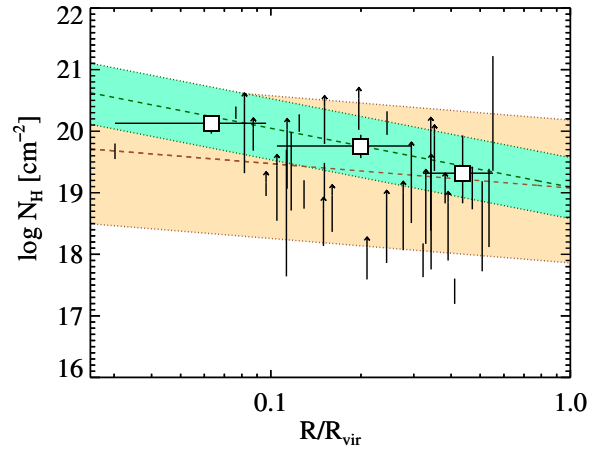


Figure 8. Total hydrogen column from the CLOUDY modeling vs. impact parameter in units of R/R_{vir} for 33 COS-Halos absorbers within 160 kpc of an $L \sim L^*$ galaxy. The range of allowed $\log N_{\text{H}}$ values for each of the 33 absorbers is shown as a vertical black line. Absorbers with a lower limit on their H I column densities are indicated by upward-facing arrows. We additionally divide the data in three bins of R/R_{vir} , taking the mean $\log N_{\text{H}}$ in each bin. The error bars on $\log N_{\text{H}}$ come from the 1000 trials included in the statistical analysis. A Kendall-Tau test on these data rejects the null hypothesis with a confidence of 92%. The power-law fit from a linear regression analysis on the sample of 33 absorbers with metal line detections is shown as a dotted green line, with the light green shaded area representing the 1σ uncertainty in the fit parameters. One reason the binned points and the fit seem to lie above the distribution is that over half of the absorbers show saturated H I absorption lines. The lower limits have the impact of increasing the uncertainty of the best fit declining profile, decreasing the slope, and increasing the y-intercept. The beige shaded area shows the fit that results when the 11 non-detections are included, as described in the text. (A color version of this figure is available in the online journal.)

N_{H} . The low value is based upon the H I column density from Tumlinson et al. (2013; typically the AODM column density) and the lowest possible ionization parameter allowed by the photoionization modeling. The high N_{H} value is based on the preferred H I column density and the highest possible ionization parameter allowed by the photoionization modeling. This high value is still a lower limit because of H I saturation. In the Appendix, we discuss how we determine a “preferred” H I column density. In brief, it is equivalent to the measured AODM column density, with the exception of several lower limits which have been raised to make the gas metallicity consistent with being solar or below. The value for N_{H} we adopt is calculated using the preferred H I column density and the mean $\log U$ for the full range.

Some values of N_{H} are determined to ± 0.2 dex, accounting for the systematic errors in the CLOUDY modeling, uncertainties in the derived column densities, and allowing for ~ 0.1 dex uncertainty that arises if the elemental abundance ratios are non-solar. Uncertainty in the slope of the EUVB adds an additional ± 0.3 dex of systematic error. Slopes shallower than HM2001 will yield higher ionization parameters, and steeper slopes result in smaller ionization parameters. We describe the details of the error accounting in the Appendix. The mean uncertainty in N_{H} is ± 0.5 dex. For the statistical tests and linear regression analysis described in this section, we sample a random distribution along the full “allowed” range of N_{H} 1000 times. We “censor” those sightlines for which H I is saturated, and thus include them as lower limits.

Figures 7 and 8 show the total hydrogen column density as a function of impact parameter, and are effectively gas surface-density profiles. There is a 92% chance that $\log N_{\text{H}}$ declines with impact parameter, and the implications of this trend are

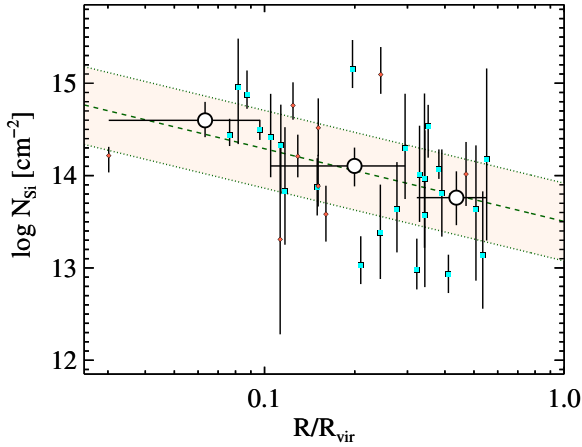


Figure 9. Total silicon column density vs. impact parameter, given as R/R_{vir} . The range of allowed $\log N_{\text{Si}}$ directly corresponds to the range in $\log U$ allowed by the data, and is shown as a vertical black line for each absorber. Red diamonds indicate a non-star-forming host galaxy, and blue squares indicate that the host galaxy is actively forming stars. We divide the data in three bins of R/R_{vir} , taking the mean $\log N_{\text{Si}}$ in each bin. The power-law fit from a linear regression analysis on the sample of 33 absorbers with metal line detections is shown as a dashed green line, with the light beige shaded area representing the 1σ uncertainty in the fit parameters.

(A color version of this figure is available in the online journal.)

discussed more fully in Section 5. Figure 7 shows this result, with blue and red data points representing star-forming and non-star-forming galaxies, respectively. Figure 8 shows the same results, limited to the modeled systems, with data divided into three bins of R/R_{vir} , and the best power-law fit with 1σ errors shown in green. We perform a survival analysis on these data by populating a random distribution along a range of allowed hydrogen column density 1000 times, and including censored data points where the H I (and thus N_{H}) is a lower limit. The best power-law fit from a linear regression analysis is:

$$N_{\text{H,preferred}} = 10^{19.1 \pm 0.5} (R/R_{\text{vir}})^{-1.0 \pm 0.5} \text{ cm}^{-2}. \quad (4)$$

We note that without the lower limits in the gas column densities, the null hypothesis is rejected with a confidence of 99%.

Additionally, in Figure 8 we show in the shaded beige area the best fit that now includes the 11 metal line non-detections. We sample the full range of allowed total hydrogen column densities for the seven systems showing H I but no metal lines. The range spans the H I column density on the lower side to the total possible N_{H} allowed by the 2σ upper limits to the metal-ion column densities on the upper side. For a typical absorber in this sample, the full range of N_{H} is $10^{15} \sim 10^{20.5}$. For the four systems that show no absorption at all, we include them at a N_{H} of 0. The best power-law fit, shown by the dashed brown line within the beige area that encompasses the 1σ error to this fit is:

$$N_{\text{H,low}} = 10^{19.1 \pm 1.2} (R/R_{\text{vir}})^{-0.4 \pm 1.3} \text{ cm}^{-2}. \quad (5)$$

Finally, we determine a total low-ion silicon column density as a function of impact parameter in Figure 9. We calculate $\log N_{\text{Si}}$ for each CLOUDY-modeled sightline by applying the ionization corrections to the low-ion metal lines we observe, and converting to silicon by assuming solar relative abundances. Since most lines of sight provide good estimates of low-ion metal column densities without saturation, this metal surface density determination is more robust than the total gas surface density determination. Metal surface density is more reliable than metallicity because it does not include uncertain H I

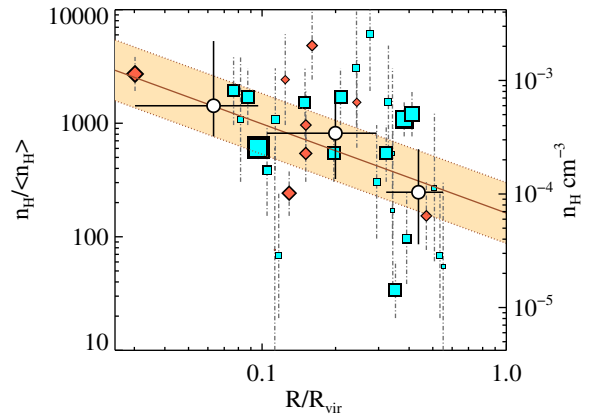


Figure 10. CLOUDY mean gas density as a function of impact parameter scaled to R/R_{vir} . We find that gas density decreases with impact parameter at a 2.3σ level. The power-law fit to the data from a linear regression analysis is shown as a brown line, with the beige shaded area represented the 1σ uncertainty of the fit parameters. The absorbers with star-forming host galaxies are shown as blue squares, while absorbers having host galaxies without any detectable ongoing star formation are shown as red diamonds. The range of density values for each absorber are shown by vertical dash-dotted gray lines, and are derived from the range in allowed $\log U$ from the CLOUDY modeling and COS data. The right axis shows the corresponding values for density in cm^{-3} . We also show the data binned in three bins of R/R_{vir} in the white circles.

(A color version of this figure is available in the online journal.)

column densities. The best power law fit from a linear regression analysis is:

$$N_{\text{Si}} = 10^{13.5 \pm 0.3} (R/R_{\text{vir}})^{-0.8 \pm 0.3} \text{ cm}^{-2}. \quad (6)$$

Peeples et al. (2014) explore the implications on the total metal mass of the cool CGM that this metal surface density implies.

Along with ionization parameters and metallicities, the CLOUDY modeling of our COS data allows us to estimate the gas volume density along each sightline, where $n_{\text{H}} = \Phi/Uc$. Here, Φ is the total flux of ionizing photons ($\sim 1.21 \times 10^4 \text{ cm}^{-2} \text{ s}^{-1}$), as defined by the Haardt & Madau (2001) background radiation field from quasars and galaxies, and c is the speed of light. This quantity n_{H} refers to the volume density of the gas that gives rise to the low-ionization-state metal lines and neutral hydrogen, and is thus not intended to represent the average volume or mass-weighted density of the CGM. The range of allowed n_{H} directly results from the range of allowed gas ionization parameters. In Figure 10, we show this gas number density, parameterized to the cosmic mean density of hydrogen at $z \sim 0.2$ of $3.3 \times 10^{-7} \text{ cm}^{-3}$, as a function of impact parameter scaled to the galaxy virial radius. Reflecting the increase in ionization parameter with R (Figure 4), there is an indication of declining gas volume density with distance from its host galaxy. A Kendall-Tau test rejects the null hypothesis at the 2σ level, and the best power-law fit is:

$$n_{\text{H}}/\langle n_{\text{H}} \rangle = 2.2 \pm 0.25 (R/R_{\text{vir}})^{-0.8 \pm 0.33}. \quad (7)$$

4.2. Total Mass of the Photoionized CGM

We have shown that the photoionized gas in the CGM of $L \approx L^*$ galaxies out to 160 kpc is highly ionized, where the mean neutral gas fraction is $\sim 1\%$. The total covering fraction of the gas is $90\% \pm 4\%$ at $N_{\text{H}} > 10^{14} \text{ cm}^{-2}$ (Thom et al. 2012; Tumlinson et al. 2013; Werk et al. 2013). Here, we estimate the total contribution of the photoionized CGM to the baryonic budget of

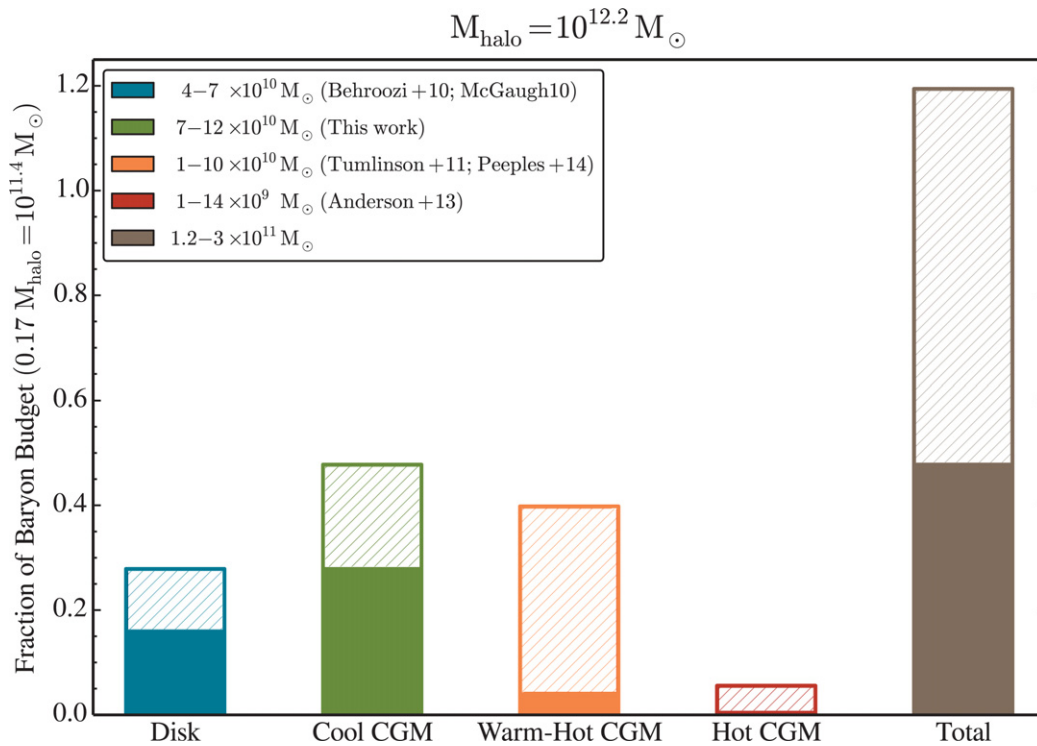


Figure 11. Baryonic budget ($0.17 M_{\text{halo}}$) of the fiducial COS-Halos galaxy, at $L \approx L^*$, represented as a bar chart showing the most massive baryonic components of the galaxy. The solid filled bars are lower limits to the fraction each component will contribute, while the hatched area above the solid bars shows potential additional contributions allowed by the data. The stars and gas in the disk of the galaxy (green) make up between 14% and 24% of the total budget, with the stellar contribution determined from abundance matching (e.g., Behroozi et al. 2010) and the gas contribution (hatched region) estimated from H I surveys (Martin et al. 2010) and the baryonic Tully–Fisher relation (McGaugh et al. 2010, McGaugh 2012). The cool CGM contribution of baryons ranges between 25% and 45%. We have taken the preferred lower limit (solid blue, Section 4.2.2), and bounded it on the top end by adding a factor of three to the H I column densities of the sightlines that show saturation. The warm-hot CGM, traced by O VI, is poorly constrained, with a contribution of at least of 5% (solid orange) from very conservative assumptions regarding the ionization fraction of O VI (Peebles et al. 2014; Tumlinson et al. 2013) and assuming solar abundance, ranging up to 37% which allows for gas metallicities of down to $0.1 Z_{\odot}$. We take the contribution from hot gas at $T > 10^7$ K from Anderson et al. (2013), which ranges from 2% to 6% (red bar), depending on the distance to which the hot halo extends. The sum of these components is given by the black bar, illustrating that galaxies have anywhere between 45% and 100% of their baryons relative to the cosmological fraction.

(A color version of this figure is available in the online journal.)

an $L \approx L^*$ galaxy treating the COS-Halos sightlines as probes of a single “fiducial” galaxy halo. This method leverages the careful, unbiased sample selection of COS-Halos: galaxy-quasar pairs were selected purely on the basis of galaxy properties with no foreknowledge of absorption. Effectively, we have generated the first statistical map of the CGM with 44 individual probes out to 160 kpc that allow us to calculate the mass by exploiting our knowledge of the gas surface density. This method requires no assumptions about volume-filling factors and cloud sizes, and relies only on measured column densities of low-ionization state metal lines and H I, along with CLOUDY-derived ionization parameters based on these quantities. In this sense, it is the first unbiased estimate of the total baryonic budget of the photoionized $L \sim L^*$ CGM, and is independent of models of halo gas density or dark-matter mass.

We make two estimates for the total mass of the CGM based on the CLOUDY modeling: a strict lower limit, and a preferred lower limit. We do so in order to account for the large systematic errors associated with our analysis, discussed more fully in the Appendix. Each calculation is described below, and relies upon converting the total hydrogen column density distribution to a gas surface density distribution by mass. For an additional mass estimate, we calculate the mass of the CGM by estimating the individual cloud sizes ($N_{\text{H}}/n_{\text{H}}$) and masses indicated by the absorption along each line of sight, and populating a CGM with these clouds to 300 kpc as is observed (Prochaska et al. 2011).

4.2.1. Strict Lower Limit

We base the strict lower limit to the baryonic mass of the photoionized, cool CGM on three very conservative assumptions regarding our data: (1) the AODM H I column density we measure from the COS spectra is the true H I column density, regardless of whether it is saturated in the data or if adopting this value requires assuming a super-solar gas metallicity; (2) the lowest ionization parameter (i.e., highest neutral gas fraction) allowed by the CLOUDY modeling is the true ionization parameter of the gas; and (3) as our observations include sightlines that only lie up to 160 kpc ($0.55 R_{\text{vir}}$) in projection from the massive host galaxy, we assume the gaseous CGM abruptly “ends” beyond this value. We include the 11 non-detections in this estimate as described in Section 4.1.

The mean total hydrogen column assuming these minimal H I values and ionization parameters is $\log N_{\text{H}} = 19 \text{ cm}^{-2}$. The best power-law fit for a gas surface density profile based on these values, truncated to 160 kpc ($0.55 R_{\text{vir}}$), is given by Equation (5). The corresponding gas surface density by mass is $1.4 m_{\text{p}} N_{\text{H}}(r)$, abbreviated here as $\Sigma_{\text{gas}}(r)$, where the factor of 1.4 corrects for the presence of helium (the other metals make a negligible contribution to the baryonic mass). It then follows that the total mass is

$$M_{\text{CGM}}^{\text{cool}} = \int 2\pi R \Sigma_{\text{gas}}(R) dR. \quad (8)$$

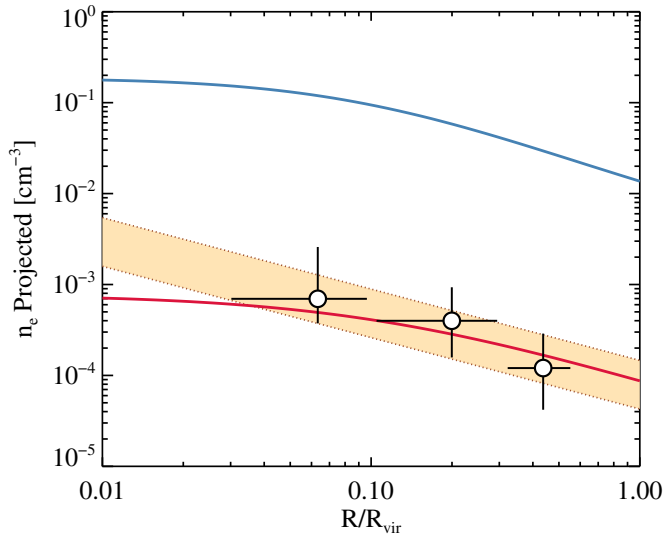


Figure 12. Projected electron density profiles for gas in a $10^{12} M_{\odot}$ halo following the formalism presented by MB04. The hot gas profile is given by the solid red curve given by Equation (12), while the cool gas profile follows the solid blue curve given by Equation (13). For comparison, we show the binned values and best fit from Figure 10 that describe our data, with hydrogen densities converted to electron densities using the ionized gas fractions of hydrogen and helium (mean correction factor of 1.16 to n_{H}). The $T \sim 10^4$ K gas we observe appears to follow the hot halo gas electron density profile rather than the cool gas electron density profile.

(A color version of this figure is available in the online journal.)

Integrating this equation from 0 to $0.55 R/R_{\text{vir}}$, we find a strict lower limit to the mass of the photoionized CGM of $2.1 \times 10^{10} M_{\odot}$.

4.2.2. Preferred Lower Limit

Adopting the AODM lower limits to $\log N_{\text{HI}}$ in some cases requires a super-solar gas metallicity, which would be significantly larger than the metallicity of the typical host galaxy disk covered by COS-Halos ($0.3\text{--}1.0 Z/Z_{\odot}$; Werk et al. 2012). Furthermore, the ionization parameters allowed by the data extend significantly higher than the minimal values (described in detail in the Appendix). We now estimate the total mass of the cool CGM based on the preferred values for $\log N_{\text{HI}}$ and $\log U$ we derive from the CLOUDY modeling and our absorption-line data. We calculate the mass in the same way as above, now excluding the 11 non-detections. In this case, the best power-law fit for a gas surface density profile based on these values is given by Equation (4).

As COS-Halos specifically targeted the inner CGM of L^* galaxies, our survey explicitly does not trace the full extent of the CGM. Data from studies that blindly probe IGM and CGM absorption and its connection to host galaxies find a gaseous extent of 300 kpc, independent of galaxy redshift and luminosity (Prochaska et al. 2011; Rudie et al. 2012). Furthermore, some metal absorbers have been shown to lie very far from the nearest galaxy, with good completeness to $L > 0.04 L^*$ (Tripp et al. 2006; Johnson et al. 2013). Accordingly, we integrate our gas surface density profile from $R/R_{\text{vir}} = 0\text{--}1$ (the mean value of R_{vir} for COS-Halos is ~ 300 kpc) to find the preferred lower limit of the mass of the photoionized CGM to be $M_{\text{CGM}}^{\text{cool}} = 6.5 \times 10^{10} M_{\odot}$. This value is still a lower limit in the sense that the H I column densities used to derive this fit are lower limits. If, for example, we find that the true H I column densities of the

saturated absorbers rise by a factor of three, then the total mass of the photoionized CGM rises to $M_{\text{CGM}}^{\text{cool}} = 1.2 \times 10^{11} M_{\odot}$.

4.2.3. Volume-filling Factor

Here, we explore the effects of approximating individual cloud sizes and deriving a volume-filling factor of the CGM. Previous work to constrain the total amount of gas in a photoionized, cool phase of the CGM has relied upon cloud counting such as this and geometrical estimations of the volume-filling factor of the clouds in extended halos (e.g., Stocke et al. 2013).

We estimate the mass in the photoionized phase of the CGM assuming that each line of sight probes one to a few gas clouds with physical properties determined by the CLOUDY modeling. We assume a cloud diameter (i.e., thickness along the line of sight), ℓ , of $N_{\text{H}}/n_{\text{H}}$ for each cloud, resulting in cloud sizes that range from 0.1 to 2000 kpc, with a median value of 10^{+35}_{-10} kpc. There is up to three orders of magnitude uncertainty in the quantity ℓ for the sightlines with the least-constrained CLOUDY solutions. For reference, Stocke et al. (2013) find a typical cloud size of ~ 1 kpc, with a range of 0.1–10 kpc using the same methodology (hence, subject to the same systematics).

In order to determine a volume-filling factor, we must estimate a shadowing factor, S (see Stocke et al. 2013 for a full explanation of this factor), which is approximately equal to an average number of discrete absorption components at separate velocities along each line of sight. Almost all of our sightlines show multiple absorbers within 600 km s^{-1} of the galaxy systemic velocity (see Section 5.3.3 for a discussion of how this impacts our mass estimate), with an average of 2.4 discrete components per line of sight when determined based on the low-ion metal lines. Because the COS spectral data have a velocity resolution of approximately 20 km s^{-1} , the number of discrete components, and thus the value of S , should be considered a lower limit. In this calculation, we also include a covering fraction, C , of 75% based on 33 of 44 sightlines showing metal line absorption with these properties, and a total extent of the CGM, R_{CGM} , of 160 kpc. We are performing this calculation solely for the inner portion of the CGM ($R < 0.5 R_{\text{vir}}$) where our data lie. We note that Stocke et al. (2013) find that this inner portion of the CGM contains approximately 75% of the total mass.

In order to calculate the mass, we must assume that the cloud properties are representative of the full population of clouds in a given L^* CGM. Furthermore, we include the full allowed range of cloud size for each absorber based on the allowed ranges of N_{H} and n_{H} . We find a volume-filling factor that ranges between 1% and 100% ($v_{\text{ff}} = C \times S \times \ell / R_{\text{CGM}}$), where the largest allowed cloud sizes are actually larger than our assumed CGM! The median value of the volume-filling factor, determined statistically with 1000 trials along the full range of allowed cloud sizes, and including lower limits, is $11^{+15}_{-9}\%$.

Assuming a geometry of spherical clouds in a spherical CGM, the total number of clouds is $N_{\text{cl}} = C \times S \times R_{\text{CGM}}^2 / \ell^2$ (Stocke et al. 2013). We find N_{cl} to range between 1 and 10^5 , with the largest clouds being the fewest in number, and the smallest clouds representing the majority of the population by design. The median value of N_{cl} is 440 ± 400 . Cloud masses, M_{cl} , range from 100 to $10^{11} M_{\odot}$, with a median value of $10^{7.6} M_{\odot}$. In this case, the median values of $N_{\text{cl}} \times M_{\text{cl}}$ give us a value of $3.2 \times 10^{10} M_{\odot}$ for the total amount of mass in the photoionized CGM within 160 kpc. This mass estimate is remarkably consistent

with the calculation of Stocke et al. (2013) for their sample of super- L^* galaxies, and our own surface-density-based estimate of the lower limit to the CGM baryonic mass.

However, the uncertainty in this estimate is very large (a factor of 10) and this calculation should be interpreted with caution. The large errors associated with this method of calculating the mass arise from the use of both N_{H} and n_{H} to calculate the cloud size. Many of our N_{H} values are lower limits, which translates to lower limits on cloud sizes (many of which are larger than 10 kpc). Such “clouds” would not fit into an L^* halo, which makes it difficult to reconcile with the observation that there are at least 2.4 discrete components per line of sight. Furthermore, the total hydrogen column and the total gas density are two quantities determined directly from the ionization parameter. At the lowest allowed volume density (i.e., highest gas ionization), the total hydrogen column is maximized, which results in a very large cloud size of hundreds to several thousands of kiloparsecs. The ranges in allowed cloud sizes for each line of sight span one full order of magnitude for the best-constrained absorbers, and three full orders of magnitude for the poorly constrained absorbers.

5. DISCUSSION

5.1. Contribution of the Photoionized CGM to the Baryonic Budget of an L^* Galaxy

The median halo mass of our sample of 44 COS-Halos galaxies, based on abundance matching, is $1.6 \times 10^{12} M_{\odot}$ (Moster et al. 2010). Thus, the cosmological baryonic budget of the typical COS-Halos galaxy is approximately $10^{11.4} M_{\odot}$ (17% of the DM component), with the stellar disk contributing approximately $10^{10.6} M_{\odot}$, or 14%. The gas in the ISM of these galaxies will vary from very little to nearly as much as the stellar contribution (McGaugh et al. 2010; Martin et al. 2010). We find that the contribution from the photoionized, bound CGM to the total baryonic budget of an $L \sim L^*$ galaxy is at least 25%—at least as much as the total contribution from the stars and gas in the disk of the galaxy.

5.2. Contribution from Additional, Unaccounted Gas Phases of the CGM

Studies of warm-hot gas phases of the CGM indicate that 10^5 – 10^7 K gas likely comprises an additional, significant contribution to the baryonic content of galaxy halos (e.g., Tumlinson et al. 2011; Tripp et al. 2011; Anderson et al. 2013; Fox et al. 2013; Meiring et al. 2013). For example, our best CLOUDY models that fit the low ionization state metal absorption lines systemically underestimate the column density of O VI measured from our COS data (mean $\log N_{\text{O VI}} = 14.5 \text{ cm}^{-2}$), as described in Section 3 and shown in the figures in the Appendix. As a result, our best models require that the majority of the observed O VI lie in a separate, more highly ionized gas phase which is consistent with the findings of previous studies. The mass estimates of this more highly ionized phase traced by O VI absorption are complicated by the lack of any additional metal line transitions near the ionization potential of O VI in the COS-Halos data. Tumlinson et al. (2011) estimate a lower limit to be $>10^9 M_{\odot}$, based on the maximum possible value for the ionization fraction of O VI ($f_{\text{O VI}} < 0.2$) and solar metallicity. Peebles et al. (2014) have refined this estimate by considering grids of simple one-dimensional halo models that account for the observed O VI, where the temperature ranges from 10^4 to 10^6 K, and the gas surface density profile drops as $(R/300 \text{ kpc})^{\alpha}$ with

alpha values of -1 and -2 . The typical value for the mass of the O VI-traced CGM is several times higher than the lower limit, and lies near $\sim 10^{10} M_{\odot}$. Thus, the O VI gas phase contributes at least 5% of the total baryons in the fiducial COS-Halos galaxy halo. For reference, if the gas is instead assumed to be $0.1 Z_{\odot}$, this mass contribution rises accordingly by a factor of 10.

The contribution of a diffuse, X-ray component to the CGM has been subject to debate, with estimates ranging from 10^9 to $10^{11} M_{\odot}$ (Anderson & Bregman 2010; Gupta et al. 2012; Anderson et al. 2013). Stacked *ROSAT* images indicate a mass of gas of $\sim 10^9 M_{\odot}$ of 5 million degree gas within 50 kpc of an L^* galaxy (Anderson et al. 2013). Extrapolating this value to 300 kpc, which may or may not be justified, is complicated by the unknown slope of the hot halo gas profile, but will increase the total mass by a factor between 6 and 14. In this estimate, the mass of the X-ray traced CGM is approximately equal to that of the O VI-traced CGM phase.

In contrast, Gupta et al. (2012) argue that the mass content of Milky Way gas at 2×10^6 K out to 160 kpc is greater than $10^{11} M_{\odot}$ based on O VII column densities from XMM Newton data of eight bright AGN and an average emission measure of the soft X-ray background (see also Fang et al. 2013). This result implicitly assumes that the O VII absorption lines and the background emission arise from the same gas phase at the same temperature and metallicity, an assumption that has generated some criticism (Wang & Yao 2012; Fang et al. 2013). Taken at face value, this estimate would mean that the X-ray traced CGM to 300 kpc could comprise at least 50% of the total baryonic budget of the Milky Way.

Finally, recent observations indicate an extensive cool, dusty component of the CGM, possibly fed by a “slow flow” of dust that has coupled with the radiation from massive stars (Zahid et al. 2013). Based on a statistical analysis of reddening using SDSS quasars behind galaxies, Ménard et al. (2010) estimate a total CGM dust mass of $\sim 5 \times 10^7 M_{\odot}$. While this does not contribute substantially to the total baryonic budget of massive galaxies, we note that this mass implies a large fraction of the total metals in the CGM are in a solid, cool phase (Peebles et al. 2014).

Summing the total contributions of all the distinct phases of the CGM, we estimate that the diffuse gas in galaxy halos accounts for at least 35% of the total baryon budget for nearby, $L \sim L^*$ galaxies. This quantity makes up more than half of the baryons purported to be missing ($\sim 60\%$). Accounting for saturation in the H I column densities used in the cool CGM calculation may raise this contribution by an additional 20%. Thus, the baryonic fraction of L^* galaxy halos may be consistent with the cosmological baryon fraction.

5.3. Hydrostatic Solutions

We now consider inferences that may be drawn on the nature of the CGM in the context of simple, hydrostatic solutions. Before proceeding, we will review the main characteristics of the CGM revealed by our COS-Halos program and previous works. First, the cool CGM is nearly ubiquitous. The covering fraction f_{C} of H I gas exceeds 90% for sightlines intersecting $0.55 R_{\text{vir}}$ (Tumlinson et al. 2013), and the incidence of lower ionization state metals is comparable (Werk et al. 2013). This material, therefore, is pervasive within the dark matter halos of L^* galaxies, but we allow that the volume-filling factor f_{V} may be small (see Section 4.2.3). Second, as emphasized in Section 4.1, the surface density of cool gas is large $N_{\text{H}}^{\text{cool}} > 10^{19} \text{ cm}^{-2}$ at essentially all impact parameters $R < R_{\text{vir}}$. Third, the cool CGM

is photoionized with $T \sim 10^4$ K. This is indicated by ratios like $\text{Si}^{++}/\text{Si}^+$ (Werk et al. 2013) and the detailed photoionization models presented here (see also Stocke et al. 2013). Fourth, the CGM of star-forming galaxies also exhibits a highly ionized phase traced by O VI (Tumlinson et al. 2011). As detailed in our Appendix, this material cannot be reproduced by the photoionization models derived to match the lower ionization states of metals observed. This O VI gas presumably traces another “phase” of the CGM. Lastly, we assume the galaxies under study exist within dark matter halos having $T_{\text{vir}} \gtrsim 10^6$ K based on the stellar mass estimates (see Section 2).

5.3.1. Single-phase Solutions

The simplest model to consider is a single-phase CGM in hydrostatic equilibrium with the dark matter halo potential. For the latter, we assume an Navarro, Frenk, & White (NFW) profile

$$\rho_{\text{DM}}(r) = \frac{\rho_s r_s^3}{r(r + r_s)^2} \quad (9)$$

defined by a scale radius r_s set by the concentration parameter $C_V \equiv r_V/r_s = 13$ and with ρ_s set by the halo mass, which we take as $M_{\text{DM}} = 10^{12} M_{\odot}$.

For the baryons, we assume the CGM is an optically thin medium, with metallicity 1/10 solar irradiated by the extragalactic UV background (Haardt & Madau 2001). We allow for a total gas mass M_g as large as $\Omega_b M_{\text{DM}}/\Omega_m$ but also consider smaller masses parameterized by f_g .

The astrophysical solutions for a baryonic plasma embedded within an NFW potential have been considered many times previously (e.g., Makino et al. 1998; Suto et al. 1998; Capelo et al. 2010), primarily in the context of hot gas around massive elliptical galaxies or the intracluster medium. Our scenario differs in that our fiducial halo is somewhat less massive and, more importantly, we consider a plasma with substantially lower gas temperature.

To simplify the analysis, we make two standard approximations: (1) the baryons do not contribute to the gravitational potential. In the extreme case, M_g may represent as much as $\Omega_b/\Omega_m \approx 0.2$ of the total mass which is a modest contribution; (2) the gas follows a polytropic law $P \sim \rho^\Gamma$. For an optically thin and photoionized gas, the temperature is relatively insensitive to the gas density. Examining the output of the photoionization models presented in Section 3 for the EUVB background and a 1/10 solar metallicity, we find that $T \propto n_{\text{H}}^{1/5}$ for $\log n_{\text{H}} \approx -5$ to -1 . This gives a polytropic index of $\Gamma = 0.8$.

We consider first the isothermal case ($\Gamma = 1$) with $T_0 = 2 \times 10^4$ K. Following the formalism of Capelo et al. (2010), the density profile is given by

$$\rho(r) = \rho_0 \exp \left[-\Delta_{\text{NFW}} \left(1 - \frac{\ln(1 + r/r_s)}{r/r_s} \right) \right] \quad (10)$$

with $\Delta_{\text{NFW}} = -\phi_0 \rho_0 / P_0 = -\phi_0 \mu m_p / k T_0$ and the central gravitational potential $\phi_0 \approx 10^5 \text{ cm}^2 \text{ s}^{-1}$ for our fiducial halo. Therefore, we have $\Delta_{\text{NFW}} \approx 1000 (T/10^4 \text{ K})^{-1}$ and the density falls off very steeply with radius resulting in a negligible value in the outer halo ($r > r_s$). We conclude that an isothermal, cool CGM cannot reproduce the observations.

For the polytropic case, we have

$$\rho(r) = \rho_0 \left[1 - \frac{\Gamma - 1}{\Gamma} \Delta_{\text{NFW}} \left(1 - \frac{\ln(1 + r/r_s)}{r/r_s} \right) \right]^{1/\Gamma-1}. \quad (11)$$

This leads to a slightly shallower density profile for $\Gamma = 0.8$ but still one where $\rho(r_s) \approx \rho_0/10^{10}$. The outer halo is very nearly a vacuum.

We conclude that a single-phase CGM with $T \approx 10^4$ K in hydrostatic equilibrium with an NFW potential cannot reproduce the observations. We are motivated, therefore, to consider more complex (and realistic) scenarios.

5.3.2. Two-phase Models

Guided by the observations for a wide range of ionization states in halo gas (e.g., Si II, Mg II, Si III, C IV, O VI), it is likely that the medium has multiple phases. In their seminal paper, Mo & Miralda-Escude (1996) introduced a two-phase model composed of cool clouds ($T \sim 10^4$ K) in pressure equilibrium with a more diffuse, hot halo gas ($T \sim 10^6$ K). They presented solutions for the density profile of the hot phase, placed constraints on the masses of the cool clouds, and tracked the dynamics (i.e., infall kinematics) of the cool clumps. In turn, they demonstrated that this two-phase model could reproduce some of the basic observables of halo gas at $z < 1$.

Other authors have since developed hydrostatic solutions in the context of high velocity clouds of the Milky Way (Sternberg et al. 2002). These treat the EUVB radiation field to model the $\log N_{\text{HI}}$ profile of the clouds and also examine higher ionization states of the gas. In all of these models, the cool phase is assumed to have “condensed” out of the hot phase via hydrostatic instabilities. While there is theoretical support for this assumption (Field 1965), other analyses have argued that galactic halos are generally stable to such condensations (Binney et al. 2009; but see McCourt et al. 2012).

In the following, we adopt the formalism of Maller & Bullock (2004, hereafter MB04), who expanded upon the Mo & Miralda-Escude (1996) treatment. Our goal is to examine whether such clumpy, two-phase scenarios reasonably reproduce the gas volume densities and surface densities estimated from our data set.

MB04 assumed that the hot gas originally follows the NFW dark matter profile (Equation (9)) with an inner core (Frenk et al. 1999). Within a characteristic cooling radius r_c , a fraction of the mass takes the form of cool, pressure-supported clouds and the hot gas evolves adiabatically to a new density profile:

$$\rho_h(x) = \rho_c \left\{ 1 + \frac{3.7}{x} \ln(1 + x) + \frac{3.7}{C_C} \ln(1 + C_C) \right\}^{3/2} \quad (12)$$

with $x = r/r_s$ and $C_C = r_c/r_s$. Given this density profile for the hot gas (and a related expression for the temperature which has a small variation), we estimate the cool gas density as

$$\rho_{\text{cool}}(r) = \rho_h(r) \frac{T_h(r)}{T_{\text{cool}}(r)} \quad (13)$$

and we adopt $T_{\text{cool}} = 2 \times 10^4$ K in what follows. All of the remaining variables relate to the assumed properties of the halo. For our fiducial model, we take $M_{\text{halo}} = 10^{12} M_{\odot}$, $r_V = 199$ kpc, $T_{\text{halo}} = 1.3 \times 10^6$ K, $C_V = 13$, and a halo gas metallicity $Z_{\text{halo}} = 0.1 Z_{\odot}$. Also, we perform the calculation at $z = 0$ but note the results are similar for any $z \ll 1$.

To compare against the measurements along the quasar sightlines which intersect halos at fixed impact parameters R , we must project the gas density profile. Because our analysis is weighted by column density (e.g., we sum all of the gas along

each sightline), we calculate a density-weighted value, which closely approximates projection effects:

$$\rho(R) = \frac{\int \rho^2(r) ds}{\int \rho(r) ds}. \quad (14)$$

The model is compared against the measurements in Figure 12, with each of our derived n_{H} values converted to an electron density based on the ionized gas fractions of hydrogen and helium. The best fit to our observations, represented by the shaded light brown area and binned data points, shows electron densities approximately two orders of magnitude below the predicted cool gas electron density profile of MB04. Counter to expectation, the data follow the hot gas electron density profile very well. Figure 12 shows that the inferred n_{H} values of the CGM lie approximately two orders of magnitude below predictions for a standard, simple two-phase scenario. Thus, in these simplified one- and two-phase cases, we have ruled out static solutions for the cool CGM.

5.3.3. The Failure of the Two-phase Solution

We now consider the robustness of this result, in particular, aspects of our analysis that impact the gas density estimates. One consideration in addressing the density discrepancy noted above is that an increase in the total integrated ionizing flux (Φ_{tot}) from the background radiation field would correspondingly increase our gas electron density measurements. This relation derives directly from the definition of U , the dimensionless ionization parameter, in which $n_{\text{H}} = \Phi_{\text{tot}}/(U \times c)$. In the Appendix, we discuss the dependence of our results on the slope and magnitude of the radiation field. We have considered both a UV background from quasars and galaxies (Haardt & Madau 2001), and the effect of adding the ionizing flux from a star-forming galaxy at a given impact parameter from our sightlines. We note that the ionization parameters are not impacted by the addition of ionizing radiation from a host galaxy, but Φ_{tot} increases with a total magnitude dependent on impact parameter ($\propto 1/R^2$), star formation rate ($\propto \text{SFR}$), and the escape fraction of ionizing photons ($\propto f_{\text{esc}}$).

An increase of two orders in magnitude in the gas densities would result if, for example, (1) the galaxy SFR exceeds $50 M_{\odot} \text{ yr}^{-1}$ for sightlines with $R < 75 \text{ kpc}$ considering an escape fraction of 5%, or (2) the SFR exceeds $20 M_{\odot} \text{ yr}^{-1}$ for sightlines at all impact parameters with $f_{\text{esc}} > 10\%$. For reference, the average SFR for the COS-Halos star-forming galaxies is approximately $1 M_{\odot} \text{ yr}^{-1}$ and the average impact parameter is 72 kpc. At our average values, assuming an f_{esc} of 1% (e.g., Inoue et al. 2006), Φ_{tot} increases by merely a factor of ~ 3 . In addition, we note that a change in the slope of the ionizing radiation field would impact our derived ionization parameters. However, physically plausible slopes above 1 ryd affect the ionization parameters at the level of ± 0.3 dex, and thus cannot be responsible for the two-order-of-magnitude discrepancy.

Another source of uncertainty in the gas densities results from modeling all of the absorption along the line of sight within $\pm 600 \text{ km s}^{-1}$ of the galaxy systemic velocity as a single phase. In reality, most of the UV-absorption data exhibit multiple component structure within this velocity range with an average of 2.4 components per absorption system seen in the lowions (see Section 4.2.3 and Werk et al. 2013). The complications of modeling each component separately are many, including: saturation in H I, making it difficult to determine $\log N_{\text{HI}}$ for each component and blending between components, complicating line fitting and hence column density measurements.

Here we comment on the effect on our derived gas densities of lumping the characteristics of many little “clouds” into one measurement. First, we consider the trend shown in Figure 2 such that lower column density gas tends to exhibit higher ionization parameters. The properties of the absorption we derive are largely dominated by the properties of the maximal component, which is the component with the highest H I column density, and, presumably, the lowest ionization parameter. Any lower density components along the line of sight typically do not drive the solutions we derive from our Cloudy modeling. Thus, if a bias exists in our results, it is a bias toward lower ionization parameters and higher gas volume densities, the opposite trend we would need in order to reconcile our observations with the MB04 two-phase solution.

In light of these considerations, we conclude that a two-phase model composed of cool clouds ($T \sim 10^4 \text{ K}$) in pressure equilibrium with virialized hot halo gas ($T \sim 10^6 \text{ K}$) is a poor description of the origin of the 10^4 K CGM at $z \sim 0$. In a linear analysis of an MB04 scenario, Binney et al. (2009) notes that unless the entropy profile of the hot ambient halo gas is very flat, any cool cloud that might condense out of it would be disrupted before they could cool by the buoyancy of thermally unstable gas. However, non-linear perturbations, such as those that may result from filamentary cold flows, do allow for cool clouds to form at densities $> 10^{-3} \text{ cm}^{-3}$ (McCourt et al. 2012; Joung et al. 2012). While this density is closer to matching those indicated by our observations, it still exceeds them by an order of magnitude. Thus, the gas densities we derive for our absorption line systems are very difficult to reconcile with this simple two-phase picture, and we must consider a different physical description of the gas.

5.4. Constraints on the Origin and Nature of the Cool CGM

Here, we explore whether the CGM gas masses and densities we measure are consistent with the gas having originated in a wind from the central host galaxy. Several recent cosmological simulations that examine the CGM incorporate various feedback prescriptions, yet all of them indicate that most of the observed absorption in the halos of galaxies is due to gas that is, or was at some point, in a galaxy-scale wind (Shen et al. 2012; Stinson et al. 2012; Joung et al. 2012; Cen 2013; Ford et al. 2013; Hummels et al. 2013). Furthermore, Cen (2013) predict that over half of the gas within 150 kpc is in the cool 10^4 K phase, consistent with our observations. The idea that winds eject a substantial amount of material into galaxy halos is echoed at least in part by the recent finding that galaxies themselves seem to be missing over half of the metals their stars have produced over the course of their lives (Zahid et al. 2012; Peebles et al. 2014). Toward galaxies themselves, the imprinted signatures of inflows and/or outflows on absorption line profiles have been studied over the last decade for modest samples of individual galaxies (e.g., Heckman et al. 2000; Martin 2005; Rubin et al. 2011), in co-added spectra of many galaxies (e.g., Weiner et al. 2009; Bordoloi et al. 2013), and most recently, for a few hundred galaxies with *HST* imaging (Martin et al. 2012; Rubin et al. 2013). These studies have shown that the Doppler blueshift of Mg II or Fe II absorption (indicative of outflows) in a galaxy spectrum is stronger with higher SFRs, is more common for galaxies that are oriented face-on, and that such outflows have the capacity to transport a significant amount of mass into the CGM and are likely to be highly collimated.

Based on absorption line profiles of Mg II and Fe II for 105 individual star-forming galaxies at $0.3 < z < 0.7$, Rubin et al.

(2013) estimate a mass outflow rate of at least $1 M_{\odot} \text{ yr}^{-1}$. Assuming the outflow rate remains constant from $z \sim 1$ to 0, and that none of the material is re-accreted, this rate implies over $10^{10} M_{\odot}$ of cool, photoionized material in the CGM of present-day galaxies, consistent with our estimates for the mass of the cool CGM. Additionally, the implied total metal mass of the CGM is roughly equivalent to the metal deficiencies determined analytically for L^* galaxies (Zahid et al. 2012; Peebles et al. 2014). Thus, the simple, seemingly self-consistent picture that emerges is one in which most of the cool gas observed in the halos of galaxies originates from the galaxy itself, building up over time to create a massive reservoir of 10^4 K halo gas.

In light of the gas densities indicated by the photoionization modeling, however, this simple picture unravels. Gas densities between 10^{-4} and 10^{-3} cm^{-3} such as we determine are not only inconsistent with the MB04 two-phase model, but are also at least an order of magnitude lower than most cosmological simulations seem to require for the cool clouds to survive on cosmological timescales. Regardless of the feedback prescription and origin, simulations of the CGM at all redshifts typically predict that the cool, 10^4 K gas is at least 10^{-2} cm^{-3} (Stinson et al. 2012; Shen et al. 2012; Cen 2012; Hummels et al. 2013). Effectively, the problem amounts to a lack of pressure support. At densities below 10^{-2} – 10^{-3} cm^{-3} , cool clouds do not survive longer than several million years (Joung et al. 2012). Thus, it appears that at the densities we measure, the gas would not survive on gigayear timescales, slowly assembling into a massive reservoir of cool circumgalactic gas. However, recent work by Ford et al. (2013) indicates that low ionization state metal lines primarily arise from so-called recycled outflows—gas that has been ejected, re-accreted, and ejected again from the central galaxy. The typical density of recycled material in this simulation is $>10^{-2} \text{ cm}^{-3}$ within 30 kpc, but consistent with 10^{-3} – 10^{-4} beyond these innermost regions. They claim that because the gas is not in hydrostatic equilibrium, it is falling back down onto the galaxy. In this picture, much of the low-ionization state material was enriched at early times and ejected to distances far from the galaxy (into the IGM), and is now falling back down. Our results are not inconsistent with this picture.

Owing to the details of the sample selection, COS-Halos galaxies are typically fairly isolated compared to the general population at $z \sim 0.2$ (Tumlinson et al. 2013; Werk et al. 2012). As a final note, we point out that group environments significantly complicate any interpretation on the origin of the CGM since absorption profiles are typically kinematically very complex (Aracil et al. 2006; Tripp 2008; Burchett et al. 2013; Stocke et al. 2014). Galaxy environment and interactions surely play some role in the observed properties of the CGM (Chen et al. 2010a; Yoon & Putman 2013), though a comprehensive study of the role of environment has not yet emerged. Finally, the absence of O VI and yet the presence of cool gas in the halos of non-star-forming galaxies (Tumlinson et al. 2011) remains a puzzle, though may be due to different origins for cool and warm-hot halo gas (Ford et al. 2013).

6. SUMMARY AND CONCLUSIONS

We have assessed the physical conditions and mass of highly ionized, cool ($T \approx 10^4$ K) CGM gas observed within 160 kpc of low-redshift, $L \approx L^*$ galaxies drawn from the COS-Halos survey. The column densities of H I and low-ionization state metal absorption lines require a characteristic total hydrogen column density of $N_{\text{H}} > 10^{19} \text{ cm}^{-2}$ in the CGM of these galaxies

(Section 4.1; Figure 7). We have leveraged our unique data set of 44 COS spectra of quasars selected to be within 160 kpc of the nearest L^* galaxy to construct the first maps of the physical state of the CGM at low redshift. Our key findings are as follows.

1. There is a 4σ anti-correlation between ionization parameter and H I column density (Section 3.1; Figure 2). The low-ionization state metal line column densities also follow this trend (Figure 3). This result is qualitatively consistent with photoionized clouds in hydrostatic equilibrium where higher column density clouds have a greater total gas volume density.
2. We find a 2σ correlation between ionization parameter and the projected distance from the galaxy (Figure 4), which is driven by a declining gas volume density with impact parameter (Figure 10). Gas is more highly ionized further from the host galaxy because the gas is lower density at large radii, and thus less shielded from the EUVB.
3. We construct gas surface density profiles of hydrogen (Figure 8) and metals (Figure 9), and find they decline out to 160 kpc ($0.55 R/R_{\text{vir}}$) with power-law slopes of -1.0 ± 0.5 and -0.8 ± 0.3 , respectively (Section 4.1). These 2σ correlations are derived from a survival analysis including censoring in the H I column densities (lower limits).
4. We provide a strict lower limit to the total mass of material in the CGM of low-redshift L^* galaxies (Section 4.2.1). This limit does not allow for line saturation and truncates at 160 kpc. There is at least $2 \times 10^{10} M_{\odot}$ of cool material in the CGM of these galaxies in the most conservative limit.
5. We provide a more realistic lower limit to the mass of low ionization state material in the halos of $L \approx L^*$ galaxies that allows for line saturation in H I (lower limits) and extends to 300 kpc: $M_{\text{CGM}}^{\text{cool}} > 6.5 \times 10^{10} M_{\odot}$ (Section 4.2.2). We emphasize that this mass estimate is a lower limit because of saturation in the H I absorption lines for over half of our sample. This mass of material suggests that over 25% of the baryon budget of an $L \approx L^*$ halo is accounted for by cool, photoionized gas in the CGM. When we sum the conservatively estimated contributions from observed hotter, more highly ionized gas phases (O VI, X-ray), we conclude that galaxies may not be baryon-depleted at all relative to the cosmological baryon fraction (Figure 11).
6. Finally, we analyze our derived gas volume densities in the context of simple hydrostatic one- and two-phase models (Section 5.3). Each of these models predicts higher gas volume densities by at least a two orders of magnitude. We conclude that the gas we observe is not in hydrostatic equilibrium with a hot gas phase at the virial temperature of the galaxy halo (Figure 12). There may be other means of supporting this gas (e.g., turbulence, magnetic fields), or else the very large amount of gas we observe has no support at all and is very short-lived in its observed state, such as might occur if it is cycling to and from galaxies on timescales that are very short compared to the dynamical times of dark matter halos.

We thank the referee, Gary Ferland, for very constructive comments and suggestions that improved this manuscript. Support for this work was provided by NASA through program GO11598, and through Hubble Fellowship grant No. 51332 from the Space Telescope Science Institute, which is operated by the Association of Universities for Research in Astronomy, Inc., under NASA contract NAS 5-26555. Optical data used in this study were obtained at the W. M. Keck Observatory,

which is operated as a scientific partnership among the California Institute of Technology, the University of California and the National Aeronautics and Space Administration. The Observatory was made possible by the generous financial support of the W. M. Keck Foundation. The authors wish to recognize and acknowledge the very significant cultural role and reverence that the summit of Mauna Kea has always had within the indigenous Hawaiian community. We are most fortunate to have the opportunity to conduct observations from this mountain. J.K.W. especially thanks Bill Mathews, Jabran Zahid, Mike Anderson, Josh Peek, Gwen Rudie, Mary Putman, James Bullock, John Stocke, Mike Shull, and Joel Bregman for very useful discussions related to this work and comments on early drafts. MSP acknowledges support from the Southern California Center for Galaxy Evolution, a multi-campus research program funded by the University of California Office of Research. Neal Katz acknowledges support from NASA ATP grant NNX10AJ95G.

Facilities: HST: COS, Keck: LRIS, Magellan: Mage

APPENDIX

DETAILS OF THE PHOTOIONIZATION MODELING

We model the ionization state of circumgalactic gas using the CLOUDY spectral synthesis code (version c13; Ferland et al. 2013), in which the gas is assumed to be a uniform slab in thermal and ionization equilibrium. We use the background radiation field from quasars and galaxies as our ionization source for gas at galactocentric distances between 10 and 160 kpc, implementing the Haardt–Madau UV background (Haardt & Madau 2001; HM2001) at $z = 0.2$ in our CLOUDY inputs. We examine the outputs of a photoionization model grid to find the set of models that are consistent with the constraints set by the ionic column densities determined from the observations. Our models vary gas metallicity, $\log N_X/N_H - \log (X/H)_\odot$, between 0.001 and the solar value (Asplund et al. 2009), and the ionization parameter, $\log U = \log n_\gamma/n_H = \text{ionizing photon density/total hydrogen number density (neutral + ionized)}$ between -1 and -5 . All of the measurements of and limits on the low-ionization metal lines that comprise this analysis (primarily Si II, Si III, C II, C III, N II, N III, O I, and Mg II) are detailed, tabulated, and provided in Werk et al. (2013).

A.1. The Addition of Ionizing Radiation and Cosmic Rays from a Central Star-forming Galaxy

We examined a similar model grid that incorporates the addition of ionizing photons from the central galaxy to the Haardt–Madau UV background as our input CLOUDY spectrum. We show the spectra of these sources of ionization in Figure 13 for reference. Although the radiation from the starburst99 galaxy spectral energy distribution (SED; Leitherer et al. 1999; $d = 72$ kpc; $\text{SFR} = 1 M_\odot \text{ yr}^{-1}$; both median values for the COS-Halos galaxy sample; Werk et al. 2012) dominates the HM2001 UV background, the slopes of the SEDs between 1 and 4 ryd are very similar. The extent to which the galaxy SED dominates HM2001 depends on the escape fraction of ionizing photons (assumed to be 5%), the distance from the galaxy, and the SFR of the galaxy. Since the influence of the galaxy radiation field scales as SFR/d^2 , we explored a wide range of parameter space for this additional ionization source. The total contribution to the ionizing radiation field increases substantially with lower impact parameter and higher SFR, dominating the extragalactic UV background radiation field below ~ 50 kpc for modest SFRs ($\text{SFR} < 1 M_\odot \text{ yr}^{-1}$). The overall slopes of the HM2001 and

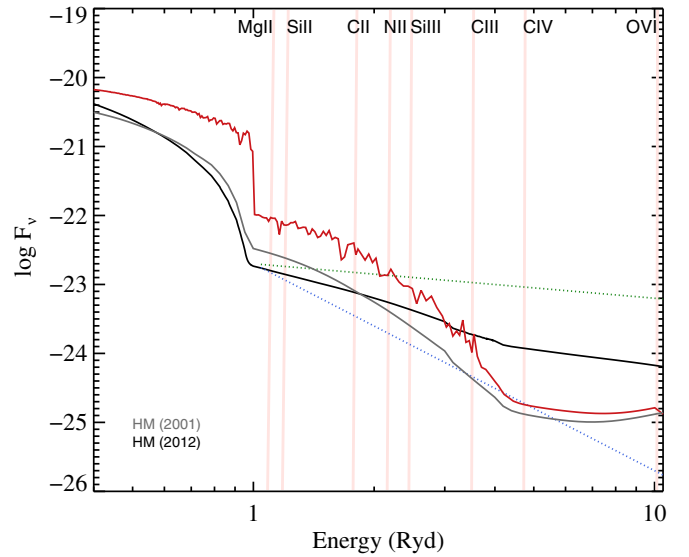


Figure 13. Several spectral energy distributions for the ionizing background radiation field: The HM2001 UV ionizing background radiation field from quasars and galaxies (dark gray), the Haardt & Madau (2012) UV ionizing background radiation field from quasars and galaxies (black line), and a galaxy SED from Starburst99 added to the HM2001 background (red). We chose the galaxy to have properties of a typical COS-Halos target galaxy, with an SFR of $1 M_\odot \text{ yr}^{-1}$, 72 kpc from the gas cloud, and with an escape fraction of ionizing photons of 0.1. We show the ionization potential energies of several common metal ions used in our analysis as vertical rose-colored lines. For the analysis described in the Appendix, we apply the HM2001 ionizing background only. We investigated the effects of including escaping ionizing radiation from a nearby galaxy, as well as varying the slope of the spectrum above 1 ryd. We analyzed both a shallow slope, with a power law exponent of -0.5 (green dotted line), and a steep slope with a power law exponent of -3.0 (blue dotted line). For reference, the HM2012 spectrum (black line) has a power law index of -1.57 above 1 ryd. Ultimately, we determine that uncertainty in the EUVB radiation field contributes systematic error in our analysis of ± 0.3 dex.

(A color version of this figure is available in the online journal.)

S99 SED spectra remain approximately equivalent over the 1–4 ryd range. The only effect of including ionizing photons from the central galaxy on our results is to push the derived ionization parameter at most ~ 0.5 dex higher at column densities below $\sim 10^{16.5} \text{ cm}^{-2}$, which modestly increases the estimate of the total amount of gas (neutral + ionized) in the CGM.

Within a galaxy virial radius, cosmic ray heating could be a significant supplemental heating and ionization source to photoionization (Wiener et al. 2013). Additionally, cosmic ray feedback theory has shown that cosmic rays may impart a significant amount of momentum to the ISM in a direction away from the galaxy, potentially driving a large-scale galactic wind (Socrates et al. 2008). At some low value of the gas volume density, heating due to the cosmic ray background (CRB; $H_{\text{CRB}} \propto n_H$) becomes more important than photoelectric heating due to the EUVB ($H_{\text{EUVB}} \propto n_H^2$). Thus, there would be a corresponding minimum gas density below which the CGM gas succumbs to a CRB-driven thermal runaway to extremely high, nearly relativistic temperatures. We may assess the contribution of the CRB to the heating of CGM gas using the built-in CRB in C13, which is based on observations of H_3^+ in the diffuse ISM of the Milky Way (Indriolo et al. 2007). The local CRB can constitute as much as 85% of the total heating for a gas volume density of $10^{-3.5} \text{ cm}^{-3}$ and 50% of the total heating for gas volume density of $10^{-2.5} \text{ cm}^{-3}$, but these numbers are highly uncertain given the large uncertainty in the local CRB. Nonetheless, these contributions imply that at the low gas densities we derive, we

may be very close to a CRB-driven thermal runaway. Thus, if the CRB in the CGM of L^* galaxies is similar to the local background, then heating due to cosmic rays could have a significant impact on the results we present here.

A.2. Systematic Uncertainty Arising from Uncertainty in the Slope of the EUVB

To carry out our analysis, we used the HM2001 EUVB spectrum from galaxies and quasars for ease of comparison with previous results. Yet, Haardt & Madau (2012, hereafter HM2012) have updated their 2001 synthesis models with the addition of several new components. We show the 2012 updated HM EVUB (HM2012) as a black line in Figure 13. There are significant differences between HM2012 and HM2001. Most notably, HM2001 exhibits a lower UV flux above ~ 1.5 ryd, smaller spectral breaks at 1 and 4 ryd, and a flatter soft X-ray spectrum. These differences arise primarily because of reduced H I and He II Lyman continuum absorption from a “sawtooth modulation” by the Lyman series of H I and He II that becomes more pronounced with increasing redshift. At low redshift, the differences between HM2001 and HM2012 are less pronounced than at high redshift.

The most important difference for our purposes is that the spectral slope of HM2001 at $z \sim 0.2$ declines more steeply between 2 and 4 ryd than that of HM2012 (shown in Figure 13). Below 2 ryd, the slopes of HM2001 and HM2012 are approximately the same. Above 4 ryd, HM2001 is flatter than HM2012. Thus, compared to HM2012, HM2001 is underproducing ions like Si III and C III relative to the lower ionization potential ions (Mg II and Si II are just above 1 ryd in Figure 13). Thus, gas ionization parameters need to be higher for HM2001 to produce the observed Si III and C III column densities. Repeating our analysis with HM2012 generally has the effect of systematically lowering our gas ionization parameters by between 0.1 and 0.4 dex. Additionally, with our prior that gas not be super-solar, the new “preferred H I” must be raised by 0.2–0.4 dex for the cases in which this prior comes into play. If the H I is known, the preferred metallicity must be raised by 0.2–0.4 dex to be consistent with ionic column densities of higher ionization state ions.

The change in the range of $\log U$ varies on a sightline by sightline basis and depends on which ions are used for the solution. For instance, sightlines that rely on Si II/Si III for the determination of $\log U$ do not change significantly when re-analyzed with HM2012 because Si III has a an ionization potential of just over 2 ryd, which is very close to where the slopes of HM2001 and HM2012 start to diverge. On the other hand, sightlines that rely on C II/C III to estimate $\log U$ exhibit a greater change in their determined $\log U$ values because the ionization potential of C III falls at an energy where the slopes of HM2012 and HM2001 are most different.

In Figure 13, we show with blue and green dotted lines a range of physically plausible slopes of the EUVB above 1 ryd. We have varied the slope of the EUVB above 1 ryd with power law exponents between -0.5 (green) and -3.0 (blue) to assess an overall systematic error in our methodology. In general, a shallower slope of the EUVB tends to decrease the best-fitting ionization parameter to the measured ionic column densities of adjacent low-ions. However, the best fitting H I column density (for cases in which the AODM lower limits would give rise to a super-solar gas metallicity) also rises equivalently for many sightlines. The average systematic error in $\log U$ that arises from uncertainty in the slope of the EUVB is ± 0.3 dex, on average.

The effect on the baryonic mass estimate is less pronounced. For example, a the total baryonic mass estimates of the cool CGM are a factor of 2.4 lower when we do the analysis with the shallowest slope considered (green dotted line in Figure 13, power law exponent of -0.5) than the steepest slope considered (blue dotted line in Figure 13, power law exponent of -3.0). Using HM2012 lowers our baryonic mass estimates made with HM2001 by a factor of 1.25. We also examined models with non-equilibrium cooling and collisional ionization equilibrium from Gnat & Sternberg (2007), neither of which offer solutions consistent with our low-ion absorption line data.

A.3. Additional Sources of Uncertainty

A similar analysis incorporating CLOUDY modeling of absorption line data was carried out by Lehner et al. (2013) for 28 Lyman limit systems at $z < 1$, with a focus on the metallicity distribution of the gas of H I-selected sightlines. Our analysis is distinct in several important ways. First, our sample selection is based on the COS-Halos survey which is galaxy-selected (Werk et al. 2012; Tumlinson et al. 2013), and probes circumgalactic gas of $L \sim L^*$ galaxies at distances of 10–160 kpc from the host galaxies. As a result, we probe a larger range of H I column densities (Figure 14). Second, many of our H I column density measurements are limited by line saturation, and we do not always obtain spectral coverage of the full Lyman series. The main side effect of the uncertainty in the H I column densities is a concomitant uncertainty in metallicity measurements. Thus, we limit the bulk of our analysis to a discussion of the ionization parameter of the gas, which is mostly unaffected by the uncertainty in the H I column density. Figure 15 highlights that while the solution for the ionization parameter of the gas is the same across several orders of magnitude of H I column density, the solution for the metallicity is over 1.5 dex lower for the higher H I column density gas. Given the uncertainty in the H I measurements, the metallicity of the gas is highly uncertain. The ionization parameter, however, is mostly independent of the choice of H I and metallicity.

In this analysis, we have constrained the CLOUDY photoionization modeling with three key priors: (1) we assume solar relative abundances of the metals considered (C, N, O, Mg, Si, Fe); (2) we do not consider gas metallicities above solar; (3) we assume a $\log U$ less than -1 , corresponding to a total gas density (n_{H}) $> \sim 10^{-5.5} \text{ cm}^{-3}$. Regarding the first prior, we acknowledge the possibility of non-solar abundance ratios by up to a factor of two (i.e., from dust depletion), which could, in practice, influence the derived metal abundances by the same factor. The ionization parameter of the gas is largely unaffected by departures from solar relative abundance ratios for two reasons. The first is that we frequently obtain column densities for two or more ions of the same element. We obtain the same ionization parameters (within the uncertainty given) when we consider only same-element pairs as we do when we consider all available ions. The second is that the CLOUDY model curves of ionic column density with $\log U$ are very steep, such that small changes in relative abundances have a minimal effect on the derived $\log U$. Regarding the second prior, we also acknowledge the possibility of super-solar circumgalactic gas metallicities, for example, in material recently ejected by a galaxy wind, or material stripped from a nearby interacting galaxy. In general, the COS-Halos sample was selected against galaxies with any indication of a recent merger event (Tumlinson et al. 2013), though at redshifts > 0.1 , it can be difficult to obtain the detailed morphological measurements necessary to rule them out

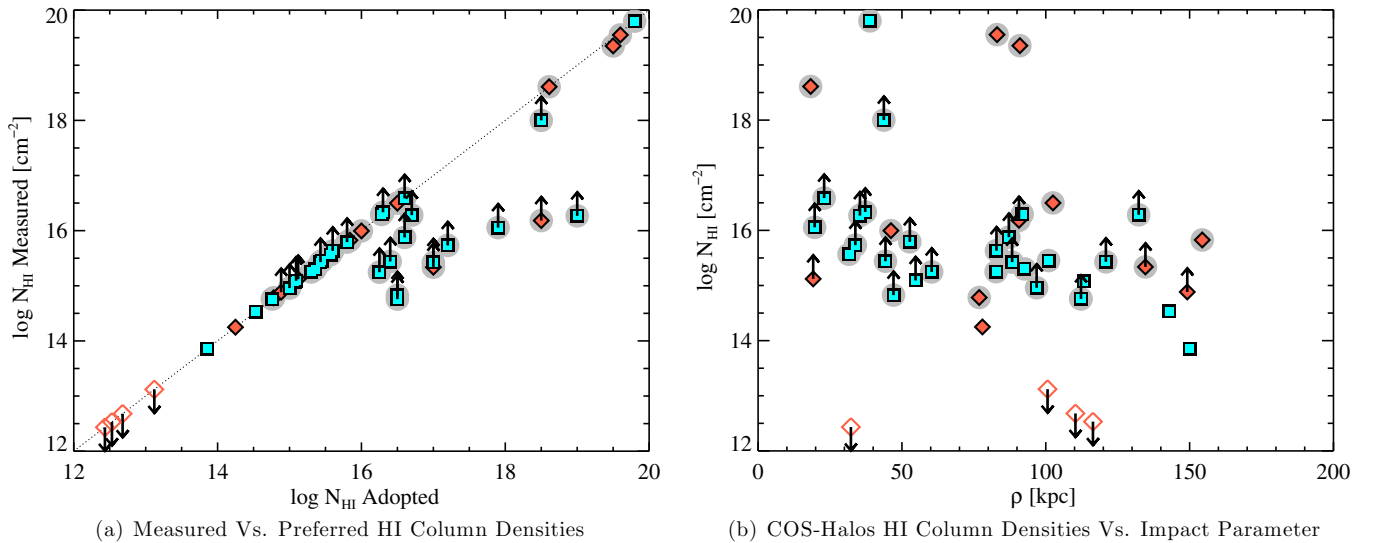


Figure 14. Two panels showing (a) the H I values adopted in this analysis, and (b) the distribution of the H I column densities with the projected distance of the quasar sightline from the galaxy (R). We show the 33 sightlines included in our photoionization modeling analysis highlighted with light gray circles. As a practical matter, when $\log N_{\text{HI}}$ falls below 10^{15} cm^{-2} , we are unable to assess the ionization state of the gas because there are no detected transitions of metal ions (Werk et al. 2013). Since most of the H I column densities from the COS-Halos data are lower limits owing to line saturation (see Tumlinson et al. 2013), we must sometimes adopt an additional nominal (“preferred”) value of the H I column density to perform the CLOUDY analysis. We detail our prescription for choosing a “preferred” H I value in the Appendix, on a sightline-by-sightline basis. In general, we assumed a column density as low as possible that would be consistent with the observed absorption line strengths and physical limitations on the gas metallicity and ionization state ($0.001 < Z/Z_{\odot} < 1$, and $-5 < \log U < -1$). Ultimately, the sightlines we incorporate in our analysis span the full range of COS-Halos impact parameters, from 10 to 160 kpc.

(A color version of this figure is available in the online journal.)

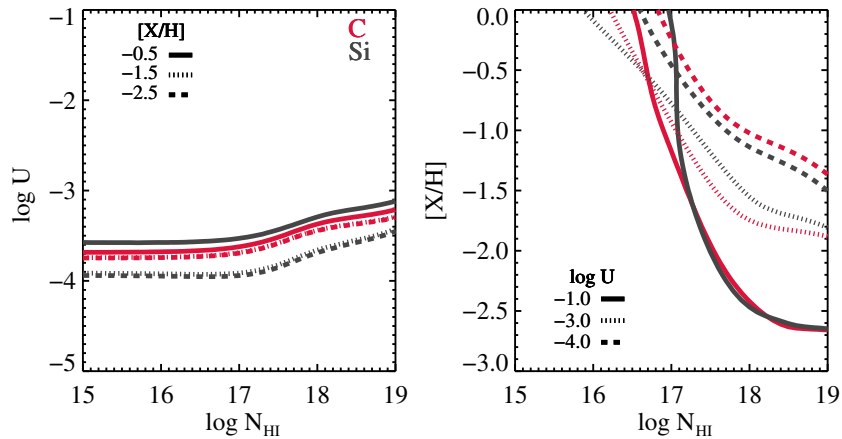


Figure 15. $\log U$ vs. $\log N_{\text{HI}}$ (left) and $[\text{X}/\text{H}]$ vs. $\log N_{\text{HI}}$ (right) for CLOUDY grids at the typical column densities and ionic ratios for C II and C III and Si II and Si III. On the left, we have shown several values of $[\text{X}/\text{H}]$, for reference, though the metallicity scarcely seems to affect the independence of $\log U$ with $\log N_{\text{HI}}$. $\log U$ is determined almost entirely from the ionic ratios of different ionization states of metal absorption lines. On the right, we show several values of $\log U$ in this parameter space which highlights that $[\text{X}/\text{H}]$ becomes more dependent on $\log N_{\text{HI}}$ with increasing ionization parameter. Regardless of the ionization parameter, $[\text{X}/\text{H}]$ is strongly dependent on the H I column density.

(A color version of this figure is available in the online journal.)

completely. We note that none of our systems analyzed require super-solar abundances, and many of them do not allow it given the measured ionic ratios. This constraint affects approximately one-fifth of our estimates on the ionization parameter, providing a lower bound to our estimate of $\log U$ (and thus $\log N_{\text{HI}}$) in these cases. In the following section, we note the specific cases for which this constraint comes into play. Regarding the third prior, the upper bound on $\log U$ of -1 rarely affects our analysis as most of the ionic ratios we consider require $\log U < -2$. As a rule, gas with a larger (less negative) value of $\log U$ has a greater ionized gas fraction. A greater ionized gas fraction, in turn, implies a greater total mass of gas contained in the CGM

of $L \sim L^*$ galaxies. Thus, this limitation, if it has any impact on our analysis, has the effect of making our final mass estimates more conservative.

In cases of saturated H I absorption lines, we attempt to place additional constraints on the H I column density limits from the COS-Halos survey in several ways, described in detail in the sightline-by-sightline analysis, and summarized broadly here. In general, we assume the lowest value of the H I column density allowed by the COS data (Thom et al. 2012). To obtain an additional upper limit on the H I column density, we determine whether the H I absorption line profile shows the presence of visible damping wings, the production of which generally occurs

at column densities greater than $10^{18.5} \text{ cm}^{-2}$. In the absence of damping wings, we place this additional upper limit on H I column densities. Second, we incorporate an allowed range of Doppler b values, parameterizing the width of the absorption components to be between 1 and 70 km s^{-1} and model the Voigt profiles of the observed H I absorption lines within the allowed range of values. This limitation is most valuable in placing additional lower limits on the H I column density, where a single saturated component cannot have a b value greater than 70 km s^{-1} . This analysis is consistent with the fits to the H I absorption lines presented in Tumlinson et al. (2013), which often give column densities above the simple AODM method determinations. Though we do not limit ourselves to the results of the Voigt profile fitting, we are guided by them. Finally, on a case by case basis, we examine the column densities of the low ionization state metal absorption lines to see if their strengths are consistent with our model grid ranges for the adopted H I value. In general, we choose a value for the adopted H I to be as low as it can be while being consistent with the line profile fits presented by Tumlinson et al. (2013) and the requirements outlined above. We show these adopted values as they compare to the COS-Halos AODM column densities in Figure 14(a). Overall, these conservative choices mean our overall mass estimate for the CGM of L^* galaxies will also be conservative.

A.4. Notes on Individual Lines of Sight

The figures shown below, beginning with Figure 16, for each system display a cross section of the CLOUDY grid at the preferred $\log N_{\text{H I}}$ and $[X/H]$ determined by examining the absorption present in the COS data for each sightline and comparing it against our CLOUDY grid of output models in several different parameter spaces. These figures show the column density of the ions in the grid as a function of the most relevant quantity to our CGM mass determination, $\log U$. On the top x-axis, we show the gas volume density, $n_{\text{H}} = \Phi / U c$. Here, Φ is the total flux of ionizing photons ($\sim 1.21 \times 10^4 \text{ cm}^{-2} \text{ s}^{-1}$), as defined by the Haardt & Madau (2001) EUVB, and c is the speed of light. We hold both the H I column density and the metallicity constant at their preferred values (described above), given in the lower right of the figure. We incorporate our measured values for specific lower ionization state metal absorption lines into these figures by outlining in bold the allowed column density from the COS data over the grid column density curves. In cases where we have a good column density constraint on an absorption line, we place in bold the value plus or minus the error on the measurement. Upper and lower limits are indicated in bold over the full allowed range of column density. On all of these plots, we have placed a bright yellow stripe of the range of $\log U$ values that fit all the available data given the preferred $\log N_{\text{H I}}$ and $[X/H]$. In some cases, the stripe may appear to be larger than the intersection of the low ion column density measurements constrain it to be since we add additional uncertainty depending on how well we can constrain $\log N_{\text{H I}}$ and $[X/H]$. Here we assess each line of sight and its solution in the CLOUDY model grid, ultimately rating it with a quality flag between 1 and 5 (5 being the best, described in Section 1 of the main text body). We show O VI model lines and column density measurements for reference, but do not require that the selected ionization parameter account for the total observed column density.

We describe which metal ions are most useful in constraining the ionization parameter and metallicity, and how we arrived at our adopted H I and $[X/H]$ values, and ultimately how we constrain the ionization parameter of the circumgalactic gas.

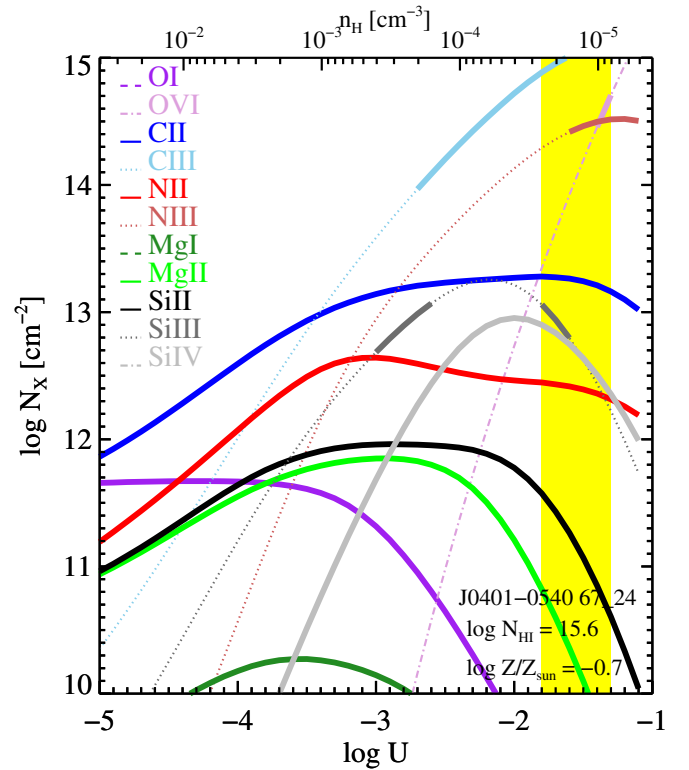


Figure 16. J0401–0540 67_24: the COS spectral data cover the Lyman series down to Ly ϵ (λ 937 Å), placing a lower limit on $\log N_{\text{H I}}$ of 15.6 since all lines are saturated, though not to a large degree. The absence of damping wings in this system lead us to adopt an $\log N_{\text{H I}}$ of 15.6. A combination of good measurements of the Si III and N III column densities, along with the lower limit on C III absorption from the saturated line at 977 Å allow us to constrain the solution for $\log U$ to be between -1.8 and -1.3 . At the preferred H I column density of 15.6, the solution for $[X/H]$ is -0.7 , constrained tightly by the small overlap region between N III and Si III column densities in the Cloudy parameter space of $\log U$ vs. $[X/H]$. If we were to adopt a higher value of $\log N_{\text{H I}}$, the solution for metallicity could drop substantially, but the solution for $\log U$ would remain near -1.5 (see Figure 15). We characterize this solution for $\log U$ as being of high quality, and thus rate it a 5.

(The complete figure set (33 images) and the color version of this figure are available in the online journal.)

Higher values of $\log U$ imply higher ionization corrections to the H I, and higher CGM mass. For our conservative mass estimate, we therefore adopt the lowest allowed $\log U$, the range of which is given in Section 4.2.1. When $\log N_{\text{H I}}$ is not well constrained by the COS-Halos data, we chose a solution for $\log U$ at the lowest $\log N_{\text{H I}}$ possible. The effect of this conservative choice often requires adopting the highest allowable value of the gas metallicity.

REFERENCES

- Anderson, M. E., & Bregman, J. N. 2010, *ApJ*, **714**, 320
 Anderson, M. E., Bregman, J. N., & Dai, X. 2013, *ApJ*, **762**, 106
 Aracil, B., Tripp, T. M., Bowen, D. V., et al. 2006, *MNRAS*, **367**, 139
 Asplund, M., Grevesse, N., Sauval, A. J., & Scott, P. 2009, *ARA&A*, **47**, 481
 Baldry, I. K., Glazebrook, K., & Driver, S. P. 2008, *MNRAS*, **388**, 945
 Battisti, A. J., Meiring, J. D., Tripp, T. M., et al. 2012, *ApJ*, **744**, 93
 Behroozi, P. S., Conroy, C., & Wechsler, R. H. 2010, *ApJ*, **717**, 379
 Bell, E. F., McIntosh, D. H., Katz, N., & Weinberg, M. D. 2003, *ApJL*, **585**, L117
 Bergeron, J. 1986, *A&A*, **155**, L8
 Binney, J., Nipoti, C., & Fraternali, F. 2009, *MNRAS*, **397**, 1804

- Blanton, M. R., Brinkmann, J., Csabai, I., et al. 2003, *AJ*, **125**, 2348
- Blumenthal, G. R., Faber, S. M., Primack, J. R., & Rees, M. J. 1984, *Natur*, **311**, 517
- Booth, C. M., Schaye, J., Delgado, J. D., & Dalla Vecchia, C. 2012, *MNRAS*, **420**, 1053
- Bordoloi, R., Tumlinson, J., Werk, J. K., et al. 2014, arXiv:1406.0509
- Bregman, J. N., & Lloyd-Davies, E. J. 2007, *ApJ*, **669**, 990
- Burchett, J. N., Tripp, T. M., Werk, J. K., et al. 2013, *ApJL*, **779**, L17
- Capelo, P. R., Natarajan, P., & Coppi, P. S. 2010, *MNRAS*, **407**, 1148
- Cen, R. 2012, *ApJ*, **753**, 17
- Cen, R. 2013, *ApJ*, **770**, 139
- Cen, R., Miralda-Escudé, J., Ostriker, J. P., & Rauch, M. 1994, *ApJL*, **437**, L9
- Cen, R., & Ostriker, J. P. 1999, *ApJ*, **514**, 1
- Chen, H., Helsby, J. E., Gauthier, J., et al. 2010a, *ApJ*, **714**, 1521
- Chen, H., & Mulchaey, J. S. 2009, *ApJ*, **701**, 1219
- Chen, H.-W., Helsby, J. E., Gauthier, J.-R., et al. 2010b, *ApJ*, **714**, 1521
- Churchill, C. W., Vogt, S. S., & Charlton, J. C. 2003, *AJ*, **125**, 98
- Danforth, C. W., & Shull, J. M. 2008, *ApJ*, **679**, 194
- Danforth, C. W., Shull, J. M., Rosenberg, J. L., & Stocke, J. T. 2006, *ApJ*, **640**, 716
- Davé, R., Hernquist, L., Katz, N., & Weinberg, D. H. 1999, *ApJ*, **511**, 521
- Davé, R., Oppenheimer, B. D., Katz, N., Kollmeier, J. A., & Weinberg, D. H. 2010, *MNRAS*, **408**, 2051
- Dekel, A., & Silk, J. 1986, *ApJ*, **303**, 39
- D’Odorico, S., & Savaglio, S. 1991, in Quasar Absorption Lines, Proc. of ESO Mini-Workshop, ed. P. A. Shaver, E. J. Wampler, & A. M. Wolfe, 51
- Dunkley, J., Komatsu, E., Nolte, M. R., et al. 2009, *ApJS*, **180**, 306
- Fang, T., Bullock, J., & Boylan-Kolchin, M. 2013, *ApJ*, **762**, 20
- Feigelson, E. D., & Nelson, P. I. 1985, *ApJ*, **293**, 192
- Ferland, G. J., Korista, K. T., Verner, D. A., et al. 1998, *PASP*, **110**, 761
- Ferland, G. J., Porter, R. L., van Hoof, P. A. M., et al. 2013, *RMxAA*, **49**, 137
- Field, G. B. 1965, *ApJ*, **142**, 531
- Ford, A. B., Davé, R., Oppenheimer, B. D., et al. 2013, arXiv:1309.5951
- Fox, A. J., Lehner, N., Tumlinson, J., et al. 2013, *ApJ*, **778**, 187
- Frenk, C. S., White, S. D. M., Bode, P., et al. 1999, *ApJ*, **525**, 554
- Froning, C. S., & Green, J. C. 2009, *Ap&SS*, **320**, 181
- Fukugita, M., Hogan, C. J., & Peebles, P. J. E. 1998, *ApJ*, **503**, 518
- Gnat, O., & Sternberg, A. 2007, *ApJS*, **168**, 213
- Green, J. C., Froning, C. S., Osterman, S., et al. 2012, *ApJ*, **744**, 60
- Gupta, A., Mathur, S., Krongold, Y., Nicastro, F., & Galeazzi, M. 2012, *ApJL*, **756**, L8
- Haardt, F., & Madau, P. 2001, in Clusters of Galaxies and the High Redshift Universe Observed in X-rays, ed. D. M. Neumann & J. T. V. Tran, **64**
- Haardt, F., & Madau, P. 2012, *ApJ*, **746**, 125
- Heckman, T. M., Lehnert, M. D., Strickland, D. K., & Armus, L. 2000, *ApJS*, **129**, 493
- Hummels, C. B., Bryan, G. L., Smith, B. D., & Turk, M. J. 2013, *MNRAS*, **430**, 1548
- Indriolo, N., Geballe, T. R., Oka, T., & McCall, B. J. 2007, *ApJ*, **671**, 1736
- Inoue, A. K., Iwata, I., & Deharveng, J.-M. 2006, *MNRAS*, **371**, L1
- Isobe, T., & Feigelson, E. D. 1986, *BICDS*, **31**, 209
- Johnson, S. D., Chen, H.-W., & Mulchaey, J. S. 2013, *MNRAS*, **434**, 1765
- Joung, M. R., Bryan, G. L., & Putman, M. E. 2012, *ApJ*, **745**, 148
- Kingdon, J. B., & Ferland, G. J. 1996, *ApJS*, **106**, 205
- Klypin, A. A., Trujillo-Gomez, S., & Primack, J. 2011, *ApJ*, **740**, 102
- Lan, T.-W., Ménard, B., & Zhu, G. 2014, arXiv:1404.5301
- Lanzetta, K. M., Bowen, D. V., Tytler, D., & Webb, J. K. 1995, *ApJ*, **442**, 538
- LaValley, M., Isobe, T., & Feigelson, E. 1992, in ASP Conference Proceedings Vol. 25, Astronomical Data Analysis Software and Systems I, ed. D. M. Worrall, C. Biemesderfer, & J. Barnes (San Francisco, CA: ASP), **245**
- Lehner, N., Howk, J. C., Tripp, T. M., et al. 2013, *ApJ*, **770**, 138
- Leitherer, C., Schaerer, D., Goldader, J. D., et al. 1999, *ApJS*, **123**, 3
- Lynds, R. 1971, *ApJL*, **164**, L73
- Makino, N., Sasaki, S., & Suto, Y. 1998, *ApJ*, **497**, 555
- Maller, A. H., & Bullock, J. S. 2004, *MNRAS*, **355**, 694
- Martin, A. M., Papastergis, E., Giovanelli, R., et al. 2010, *ApJ*, **723**, 1359
- Martin, C. L. 2005, *ApJ*, **621**, 227
- Martin, C. L., Shapley, A. E., Coil, A. L., et al. 2012, *ApJ*, **760**, 127
- McCourt, M., Sharma, P., Quataert, E., & Parrish, I. J. 2012, *MNRAS*, **419**, 3319
- McGaugh, S. S. 2008, in IAU Symp. 244, Dark Galaxies and Lost Baryons, ed. J. Davies & M. Disney (Cambridge: Cambridge Univ. Press), **136**
- McGaugh, S. S. 2012, *AJ*, **143**, 40
- McGaugh, S. S., Schombert, J. M., de Blok, W. J. G., & Zagursky, M. J. 2010, *ApJL*, **708**, L14
- Meiring, J. D., Tripp, T. M., Werk, J. K., et al. 2013, *ApJ*, **767**, 49
- Ménard, B., Scranton, R., Fukugita, M., & Richards, G. 2010, *MNRAS*, **405**, 1025
- Mo, H. J., & Miralda-Escudé, J. 1996, *ApJ*, **469**, 589
- Morris, S. L., Weymann, R. J., Dressler, A., et al. 1993, *ApJ*, **419**, 524
- Morton, D. C. 2003, *ApJS*, **149**, 205
- Moster, B. P., Somerville, R. S., Maulbetsch, C., et al. 2010, *ApJ*, **710**, 903
- Narayanan, A., Charlton, J. C., Misawa, T., Green, R. E., & Kim, T.-S. 2008, *ApJ*, **689**, 782
- Oppenheimer, B. D., Davé, R., Katz, N., Kollmeier, J. A., & Weinberg, D. H. 2012, *MNRAS*, **420**, 829
- Oppenheimer, B. D., Davé, R., Kereš, D., et al. 2010, *MNRAS*, **406**, 2325
- Oppenheimer, B. D., & Schaye, J. 2013, *MNRAS*, **434**, 1063
- Papastergis, E., Cattaneo, A., Huang, S., Giovanelli, R., & Haynes, M. P. 2012, *ApJ*, **759**, 138
- Peebles, M. S., Werk, J. K., Tumlinson, J., et al. 2014, *ApJ*, **786**, 54
- Penton, S. V., Stocke, J. T., & Shull, J. M. 2004, *ApJS*, **152**, 29
- Persic, M., & Salucci, P. 1992, *MNRAS*, **258**, 14P
- Prochaska, J. X., Chen, H.-W., Howk, J. C., Weiner, B. J., & Mulchaey, J. 2004, *ApJ*, **617**, 718
- Prochaska, J. X., Weiner, B., Chen, H.-W., Cooksey, K. L., & Mulchaey, J. S. 2011, *ApJS*, **193**, 28
- Rubin, K. H. R., Prochaska, J. X., Koo, D. C., et al. 2013, arXiv:1307.1476
- Rubin, K. H. R., Prochaska, J. X., Ménard, B., et al. 2011, *ApJ*, **728**, 55
- Rudie, G. C., Steidel, C. C., Trainor, R. F., et al. 2012, *ApJ*, **750**, 67
- Sargent, W. L. W., Young, P. J., Boksenberg, A., & Tytler, D. 1980, *ApJS*, **42**, 41
- Savage, B. D., & Sembach, K. R. 1991, *ApJ*, **379**, 245
- Schaye, J. 2001, *ApJ*, **559**, 507
- Shen, S., Madau, P., Aguirre, A., et al. 2012, *ApJ*, **760**, 50
- Socrates, A., Davis, S. W., & Ramirez-Ruiz, E. 2008, *ApJ*, **687**, 202
- Somerville, R. S., & Primack, J. R. 1999, *MNRAS*, **310**, 1087
- Sternberg, A., McKee, C. F., & Wolfire, M. G. 2002, *ApJS*, **143**, 419
- Stinson, G. S., Brook, C., Prochaska, J. X., et al. 2012, *MNRAS*, **425**, 1270
- Stocke, J. T., Keeney, B. A., Danforth, C. W., et al. 2013, *ApJ*, **763**, 148
- Stocke, J. T., Keeney, B. A., Danforth, C. W., et al. 2014, arXiv:1405.4307
- Suto, Y., Sasaki, S., & Makino, N. 1998, *ApJ*, **509**, 544
- Thom, C., & Chen, H.-W. 2008, *ApJ*, **683**, 22
- Thom, C., Tumlinson, J., Werk, J. K., et al. 2012, *ApJL*, **758**, L41
- Tripp, T. M. 2008, in AIP Conf. Ser. 1035, The Evolution of Galaxies Through the Neutral Hydrogen Window, ed. R. Minchin & E. Momjian (Melville, NY: AIP), **63**
- Tripp, T. M., Aracil, B., Bowen, D. V., & Jenkins, E. B. 2006, *ApJL*, **643**, L77
- Tripp, T. M., Jenkins, E. B., Bowen, D. V., et al. 2005, *ApJ*, **619**, 714
- Tripp, T. M., Lu, L., & Savage, B. D. 1998, *ApJ*, **508**, 200
- Tripp, T. M., Sembach, K. R., Bowen, D. V., et al. 2008, *ApJS*, **177**, 39
- Tripp, T. M., Meiring, J. D., Prochaska, J. X., et al. 2011, *Sci*, **334**, 952
- Tumlinson, J., Thom, C., Werk, J. K., et al. 2011, *Sci*, **334**, 948
- Tumlinson, J., Thom, C., Werk, J. K., et al. 2013, *ApJ*, **777**, 59
- Vasiliev, E. O., Ryabova, M. V., & Shchekinov, Y. A. 2013, arXiv:1312.4364
- Wakker, B. P., & Savage, B. D. 2009, *ApJS*, **182**, 378
- Wang, Q. D., & Yao, Y. 2012, arXiv:1211.3137
- Weiner, B. J., et al. 2009, *ApJ*, **692**, 187
- Werk, J. K., Prochaska, J. X., Thom, C., et al. 2012, *ApJS*, **198**, 3
- Werk, J. K., Prochaska, J. X., Thom, C., et al. 2013, *ApJS*, **204**, 17
- Wiener, J., Zweibel, E. G., & Oh, S. P. 2013, *ApJ*, **767**, 87
- Yang, X., Mo, H. J., & van den Bosch, F. C. 2009, *ApJ*, **695**, 900
- Yoon, J. H., & Putman, M. E. 2013, *ApJL*, **772**, L29
- Zahid, H. J., Dima, G. I., Kewley, L. J., Erb, D. K., & Davé, R. 2012, *ApJ*, **757**, 54
- Zahid, H. J., Torrey, P., Kudritzki, R. P., et al. 2013, *MNRAS*, **436**, 1852
- Zhu, G., & Ménard, B. 2013, *ApJ*, **773**, 16